Sensitivity of Off-Nadir Zenith Angles to Correlation between Visible and Near-Infrared Reflectance for Use in Remote Sensing of Aerosol over Land

C. K. Gatebe, M. D. King, S. C. Tsay, Q. Ji, G. T. Arnold and J. Y. Li

IEEE Transactions on Geoscience and Remote Sensing

Manuscript submitted June 19, 2000.

C. K. Gatebe is with the Goddard Earth Science & Technology Center, University of Maryland Baltimore County, Baltimore, MD 21228-5398.

M. D. King and S. C. Tsay are with the Earth Sciences Directorate, NASA Goddard Space Flight Center, Greenbelt, MD 20771.

Q. Ji is with Science Systems and Applications, Inc., NASA Goddard Space Flight Center, Greenbelt, MD 20771

G. T. Arnold and J. Y. Li are with Emergent Informational Technologies Inc., 2600 Park Tower Drive, Suite 1000, Vienna, Virginia 22180.

***Abstract*—** Cloud Absorption Radiometer (CAR) multispectral and multi-angular data, collected during the Smoke, Clouds, and Radiation–Brazil (SCAR-B) experiment, was used to examine the ratio technique, the official method for remote sensing of aerosols over land from the Moderate Resolution Imaging Spectroradiometer (MODIS) data, for view angles from nadir to 65° off-nadir. The strategy we used is to first select a pristine, low aerosol optical thickness flight, and computed ratios of reflectance at 0.47 and 0.68 μm to corresponding values at 2.20 μm, separately for backward and forward scattering directions. Similarly, we analyzed data from high turbidity flights for comparison purposes. For both flights, we removed the effects of atmospheric absorption and scattering using 6S, a radiative transfer code, and then recomputed the ratios again, for different values of aerosol optical thickness. Finally, we analyzed bidirectional reflection function (BRF) data to examine the dependence of the ratio technique on the relative azimuth angle. Results of this analysis show that a relationship between visible reflectance and near infrared reflectance exists for view angles from nadir to 40° off-nadir and that simple parametric relationships can be derived. In spite of these observed relationships, the relationship $R^{0.47} = R^{2.20}/4$, used in remote sensing of aerosol over land, does not seem to hold for the cases tested, both in the forward and backward scattering directions, and that $R^{0.68} = R^{2.20}/2$ seems to hold for view angles from nadir to 45° off-nadir but only in the backward scattering direction. These ratios show little variation with azimuth view angle and this seems to hold well for backward scattering directions over dark targets.

I. INTRODUCTION

For quite some time now, there has been a growing concern about the potential climatic influence of changing atmospheric aerosol loading. This concern was raised in the 1960s, when it was suggested that increasing atmospheric aerosol concentrations would scatter more sunlight back into space, thereby increasing planetary albedo and cooling the Earth [28]. It became even more worrying when studies [31], [3] speculated that increasing anthropogenic aerosol would cool the earth substantially, possibly sending it into an ice age; a notion that has since been discounted with a realization that the influence of aerosols depends on their composition, albedo of the underlying surface, and presence of clouds.

Aerosols exhibit high spatial and temporal variability, making it difficult to characterize them solely on the basis of sporadic ***in situ*** measurements [13]. For that reason, satellite remote sensing is slowly gaining worldwide recognition as a method best suited for characterizing aerosols on a global basis because of the wide spatial coverage available to satellites. The process involves decoupling the measured radiance signal into its two components, one originating from the Earth's surface and the other originating from the atmosphere [12]. By applying radiative transfer theory, aerosol optical characteristics (optical thickness, single scattering albedo, asymmetry factor, refractive index, and aerosol size distribution) can be derived from the atmospheric component. In turn, the remotely sensed aerosol information is required for atmospheric correction of satellite images of surface cover [15], [34]. However, separating the two components, surface and atmospheric reflectance, presents a formidable challenge in remote sensing of tropospheric aerosol from space, and in an attempt to overcome it, several different techniques have been proposed, each with advantages and dis-

advantages over other techniques, as reviewed by King ***et al.*** [22].

Over oceans, because of low surface reflectance, which means low contamination by the atmospheric component, remote sensing of aerosol has been quite successful (cf. [6], [29], [24], [25], [14], [9], [35], [37], [30]). However, over land, where most anthropogenic aerosol particles arise, aerosol information has been derived but with a lot of difficulties associated with decoupling the surface radiance, which is much higher than what is measured over the oceans, from the atmospheric component that contains the desired aerosol information [8], [18], [5]. In the late 1980s, in an attempt to reduce uncertainty associated with surface effects, Kaufman and Sendra [17] suggested a "dark surface target" approach to retrieve aerosol optical thickness in regions where the surface is covered by dense dark vegetation or forest. One advantage of the dark surface target approach is that the surface reflectance is small, as over the oceans, so that errors in retrieving aerosol optical thickness are relatively small when compared to errors over bright surfaces [7]. Another advantage of using the dark target approach is that there are correlations between the shortwave-IR band at 2.1 μm and visible bands in the blue and red spectral regions. Hence, the shortwave -IR band at 2.1 μm may be used to estimate the surface reflectance in the blue and red bands, and subsequently used to infer aerosol optical thickness at these two visible bands [19]. Detecting dark surface targets using 2.1 μm rather than 3.75 μm has proven to be more accurate. One advantage of 2.1 μm is that it is unaffected by thermal emission. In addition, reflected radiation at 2.1 μm is largely unaffected by aerosol particles in the atmosphere, which are generally much smaller than this wavelength (e.g., smoke, sulfates, etc), with the single exception that dust can influence reflected radiation at 2.1 μm [16]. In addition, unlike emission corrections, there is much greater certainty in correcting for the effect of water vapor

absorption once the amount of water vapor in the column is measured from the same satellite.

In a recent study, Wen ***et al.*** [41] extended the dark surface technique for use in aerosol retrieval over land when the surface reflectance at 2.1 μm is related to its counterpart at 0.47 and 0.66 μm. In this method, known as the path radiance technique, path radiance in the visible is equated to the intercept of an extrapolated linear fit of visible and shortwave-IR top of the atmosphere reflectance. This intercept describes the chosen visible band's atmospheric path radiance, from which the corresponding aerosol optical thickness can be retrieved. The method avoids using specific values of these relations as the traditional dark target approach does. So far this method, though promising, has been applied to data set from Landsat Thematic Mapper (TM) only, and will need to be validated for a much wider data set.

The intent of this paper is to examine the effect of the surface reflectance ratio technique on the retrieval of aerosol optical thickness over dense dark vegetation. We will examine the sensitivity of reflected solar radiation over a wide range of viewing angles and azimuthal directions using reflectance measurements obtained with the Cloud Absorption Radiometer (CAR) during the Smoke, Clouds, and Radiation – Brazil (SCAR-B) experiment conducted in 1995 [20]. Variations of zenith angle across images and between images occur naturally due to a wide swath width in satellite imagery, and these spectral reflectance properties of natural surfaces need to be accurately assessed in retrieving aerosol optical thickness over land using a global dataset such as the Moderate Resolution Imaging Spectroradiometer (MODIS) on the Terra platform [21]. MODIS images the Earth's surface across track with a swath width of 2330 km, with the view zenith angle varying between ±55°, or about ±61° at the surface.

II. Description of the Cloud Absorption Radiometer

The Cloud Absorption Radiometer (CAR) is a multispectral (13-channel) scanning radiometer developed at Goddard Space Flight Center, initially for the purpose of measuring the angular distribution of scattered radiation deep within a cloud layer at selected wavelengths in the visible and near-infrared. From these measurements, the spectral single scattering albedo of clouds was determined using diffusion domain method that avoids the difficulties of traditional radiometric observations [23]. Because of its multiangle viewing geometry, however, the CAR has more recently been used to measure the bidirectional reflection function (BRDF) of numerous terrestrial surfaces as described by Tsay ***et al***. [38], Soulen ***et al***. [36], and Arnold ***et al***. [2]. This is accomplished using an aircraft that banks at a comfortable roll angle of ~20° and flies a closed circular flight pattern about 3 km in diameter over a uniform surface of interest (e.g., ocean, snow, tundra, vegetation, etc.) at a constant altitude and uniform speed.

For the results presented in this paper, the CAR was housed in the nose cone of the University of Washington C-131A research aircraft, where it was designed to scan in a vertical plane on the right-hand side of the aircraft from 5° before zenith to 5° past nadir (190° aperture). The Instantaneous Field of View (IFOV) of the radiometer is 1°. To allow for the large variation in absolute magnitude of the radiance arising as a function of optical properties of the target as well as solar zenith angle, the CAR provides for seven manual gain settings that permit great flexibility in field operations by allowing the operator to apply a uniform gain adjustment to all eight electrical channels simultaneously while collecting the observations, thereby minimizing saturation of the radiometer as it scans through the sun or looks at dark targets. This manual gain setting is output to the data system and used in the conversion of counts to radiance of the

scene.

The choice of the 13 CAR channels (bands) is based on realization that there are six different water vapor absorption bands in the visible and near-infrared regions. The bands (channels) define the absorption characteristics of all water vapor window regions in the near-infrared. All the channels were selected to carefully minimize the effects of gaseous absorption, except for the UV-B channel where ozone absorption is desired.

The optical system of the CAR is nondispersive, comprising a complex configuration of dichroic beam splitters and narrowband interference filters. The CAR provides radiometric measurements at 13 discrete wavelengths that, during SCAR-B, were at 0.307, 0.472, 0.675, 0.869, 1.038, 1.219, 1.271, 1.552, 1.643, 1.725, 2.099, 2.207 and 2.303 μm. Even though there are 13 optical channels, the CAR records data at only eight spectral channels at one time. The first seven spectral channels (0.307-1.271 μm) are continuously and simultaneously sampled, whereas the eighth channel is selected from one of the six channels on the filter wheel (ranging from 1.552-2.303 μm), and is either locked on a particular channel or rotated to measure a new channel after a preset number of scans. In general the bandwidth of channels 1-7 is ~0.020 μm, whereas the bandwidth of the filter wheel channels is ~0.040 μm.

III. Theory

Kaufman *et al.* [19] showed that for many terrestrial land surfaces, including soil, sand, urban, vegetation, and forest, surface reflectance in the red $A_g^{0.67}$ is approximately half that in the shortwave infrared $A_g^{2.20}$, and the reflectance in the blue $A_g^{0.47}$ is a about a quarter of that at 2.20 μm. In other words, they found that

$$\boldsymbol{A}_g^{0.47} \sim 0.5\,\boldsymbol{A}_g^{0.67} \sim 0.25\,\boldsymbol{A}_g^{2.20}. \quad (1)$$

Using these relationships, Kaufman ***et al.*** showed that the surface reflectance in the visible bands can be predicted within $\Delta \boldsymbol{A}_g^{0.47} \sim \Delta \boldsymbol{A}_g^{0.67} \sim 0.006$ from surface reflectance measurements at 2.20 μm when $\boldsymbol{A}_g^{2.20} \leq 0.10$. This results in half the error obtained using the 3.75 μm channel, and corresponds to an error in aerosol optical thickness $\Delta\tau_a \sim 0.06$ [19]. These results, though applicable to several biomes (e.g., forests, and brighter lower canopies), have only been tested at nadir (zenith angle $\theta = 0°$). Considering the importance of these results to the remote sensing of aerosol optical thickness over land using MODIS data, it is important to assess the accuracy of this relationship for off-nadir viewing angles using CAR data.

Although there is more than one definition of the spectral bidirectional reflectance function (BRF), we use the definition of reflection function found in van de Hulst [39] and given by

$$\boldsymbol{R}^{\lambda}(\tau_a;\ \theta,\ \theta_0,\ \varphi) = \frac{\pi \boldsymbol{I}^{\lambda}(0,\ -\theta,\ \varphi)}{\mu_0 \boldsymbol{F}_0}, \quad (2)$$

where θ and θ_0 are the viewing and solar zenith angles, respectively; φ is the azimuthal angle between the viewing and illumination directions; $\mu_0 = \cos\theta_0$; $\boldsymbol{I}^{\lambda}$ is the corresponding reflected radiance; and $\boldsymbol{F}_0$ is the collimated irradiance at the top of the atmosphere.

The reflection function of a cloud-free and vertically homogeneous earth–atmosphere system overlying a Lambertian surface with reflectance $\boldsymbol{A}_g$ can be written as [4]

$$\boldsymbol{R}^{\lambda}(\tau_a;\ \theta,\ \theta_0,\ \varphi) = \boldsymbol{R}^{\lambda}_{atm}(\tau_a;\ \theta,\ \theta_0,\ \varphi) +$$

$$\frac{A_g^{\lambda}}{1 - A_g^{\lambda}\bar{r}_{atm}^{\lambda}(\tau_a)}\, t_{atm}^{\lambda}(\tau_a;\, \theta)\, t_{atm}^{\lambda}(\tau_a;\, \theta_0), \tag{3}$$

where $R_{atm}^{\lambda}(\tau_a;\, \theta,\, \theta_0,\, \varphi)$ is the reflection function, $\bar{r}_{atm}^{\lambda}(\tau_a)$ the spherical albedo, and $t_{atm}^{\lambda}(\tau_a;\, \theta_0)$ the total transmission (diffuse plus direct) when $A_g^{\lambda} = 0$. Each of these functions is explicitly a function of aerosol optical thickness and implicitly a function of aerosol size distribution and single scattering albedo. In practice, the bidirectional reflectance properties of the surface are substituted for the Lambertian reflectance A_g^{λ} when applying this expression to satellite observations.

This means that when $A_g^{\lambda}\bar{r}_{atm}^{\lambda}(\tau_a)$ is small, as is often the case over dark surfaces, the reflectance of the earth-atmosphere system is linearly proportional to the surface reflectance A_g. Under these conditions, the apparent reflectance of visible radiation can be expressed as

$$R^{vis}(\tau_a;\, \theta,\, \theta_0,\, \varphi) = R_{atm}^{vis}(\tau_a;\, \theta,\, \theta_0,\, \varphi) + t_{atm}^{vis}(\tau_a;\, \theta)\, t_{atm}^{vis}(\tau_a;\, \theta_0)\, A_g^{vis}. \tag{4}$$

In the shortwave infrared, on the other hand, atmospheric scattering can largely be ignored for most aerosol types (e.g., smoke, sulfates, etc. [19]). Under these conditions, the apparent reflectance can be expressed as

$$R^{2.20}(\tau_a;\, \theta,\, \theta_0,\, \varphi) = t_{atm}^{2.20}(\tau_a;\, \theta)\, t_{atm}^{2.20}(\tau_a;\, \theta_0)\, A_g^{2.20}. \tag{5}$$

When looking downward from a satellite, aerosol particles can readily be detected at visible wavelengths, but not at 2.20 μm. This effect may be used in the remote sensing of tropospheric aerosol. Over a dark target, such as dense dark vegetation, one can use the reflectance measured at 2.20 μm to predict the surface reflectance at visible channels. The differences between the measured reflectance and the predicted surface reflectance at a visible wavelength is due primarily to aerosol scattering and absorption [22]. Kaufman *et al.* [19] devel-

oped the empirical relationship shown in Eq. (1) based on nadir observations. In the following sections we will examine whether $k_0 = 0.25$ and 0.50, where k_0 is the constant of proportionality between reflectances at corresponding wavelengths in the blue, red, and shortwave infrared assumed by Kaufman *et al.*, and to what extent this relationship is robust for nadir as well as off-nadir viewing zenith angles.

IV. Data

To get k_0, defined above as $\rho_g^{0.47} = 0.25\,\rho_g^{2.20}$ for the 0.47 μm channel and $\rho_g^{0.67} = 0.5\,\rho_g^{2.20}$ for the 0.68 μm channel, we need a relatively clean (low optical thickness) case. We chose data from a CAR Flight on August 18, 1995 that took place 300 km north of Brasilia, Brazil during SCAR-B. Information on the spectral aerosol optical thickness obtained from a Cimel sunphotometer [11] located in Brasilia is available to do atmospheric correction for this day. For comparison purposes, we also analyzed a CAR Flight on August 27, 1995, a hazy day in Cuiabá. Each flight lasted approximately 2 hr 45 min, and included about 2000 scans obtained with the 2.20 μm channel. The aircraft flew about 500 to 5000 m above the ground during these flights. Accordingly, the footprint of the CAR is about 10 to 100 m on the ground at nadir. If the surface is homogenous, the difference between the reflectance of consecutive scans is quite small. We used some of these data to examine the relation $\rho_g^{0.47(0.67)} = k_0\,\rho_g^{2.20}$ for zenith angles from nadir to 65° off-nadir.

We have analyzed data from both flights for periods represented by 17:47–17:51, 19:18–19:23, and 19:41–19:45 UTC on August 18 and 19:02-19:08 UTC on August 27. On both days, we selected sections of the flight that appeared to be spatially homogeneous based on visual inspection of red-green-blue (RGB)

composite images of the entire flights. With the plane traveling at a nominal speed of 80 ms^{-1} and the scan mirror rotating at 100 rpm, we obtained 400-500 scans over a distance of 19.2 km for each of the time sections selected on August 18, and 600 scan lines spread over 28.8 km on August 27. With a sample being acquired every 0.6 seconds, we obtained observations at a fixed view zenith angle once every 48 m along the aircraft ground track for channels 1-7, where data are collected continuously and simultaneously. For the filter wheel, representing channels 8-13, we locked the filter wheel in a single position for extended periods of time, thereby allowing data to be acquired in a manner similar to channels 1–7. If the filter wheel is set to rotate in an automatic observation mode, each of channels 8-13 are measured for n scans, then for each channel a sample is repeated every $3.6n$ sec or after $288n$ m along the ground-track. This study required us to use data from channels 1 (blue, 0.472 μm), 2 (red, 0.675 μm), and 12 (near-infrared, 2.20 μm), so the number of data points is limited to data acquired when channel 12 was in the filter wheel position during the time limits and distance of each flight.

We have also analyzed data from August 18 and 25 acquired when the CAR was in bidirectional reflectance mode [38], where the reflectance is measured during changing azimuthal conditions, in contrast to the above cases where the azimuth direction was fixed and the CAR was scanning in a cross track direction.

V. RESULTS

Reflectance measurements in the 2.20 μm atmospheric window are least affected by most aerosol types (e.g., smoke, sulfates, etc.), whereas the atmospheric effect is significant for measurements in the visible wavelength region at

0.472 μm (blue) and 0.675 μm (red). In order to test whether a relationship exists between solar radiation at 2.20 μm and the visible (blue and red), we have plotted reflectance at 2.20 μm against reflectance at both blue and red wavelengths for zenith angles from nadir (0°) to 65° off-nadir (Figure 1). These angles have been chosen since most satellites view their targets at an angle within the range of 0° to 65°. Since the optical path is shorter at nadir, increasing at longer wavelengths, any information derived from reflectance measurements at nadir would be expected to be more accurate due to reduced uncertainty as a result of increased total optical thickness. Theoretically, the probability of a photon undergoing absorption or scattering should not be dictated by the distance between the source and the sensor, but by the density of the material in between.

On August 18, the University of Washington C-131A obtained CAR measurements between 17:47 and 17:51 UTC, when the solar zenith angle θ_0 = 45.4° and solar azimuth angle φ_0 = 304.1°. The plane was heading NNW at a heading H = 346.2° and an altitude z = 2450 m. Since the CAR scans in a vertical plane on the right-hand side of the aircraft, the relative azimuth φ = 132.1° such that the photons reflecting from the earth-atmosphere system are backscattered from the target. The position of the airplane changed from 13.36°S, 48.51°W to 13.18°S, 48.56°W, while it's altitude varied by only ~20 m. Clear weather was observed and signs of haze were largely absent; therefore this flight can be characterized as a clean one with low aerosol concentration, cloud free conditions, and aerosol optical thickness of 0.08 as measured with a sunphotometer located 300 km to the south in Brasilia.

Figure 1 shows scatter plots of reflectance in the visible channels (blue and red) as a function of reflectance in the shortwave infrared (2.20 μm) for zenith angles θ = 0°(nadir), 10°, 20°, 30°, 40°, and 65° when φ = 132.1°. Scatter plot sta-

tistics (number of points used, slope, intercept, and correlation coefficient) for zenith angles between 0° to 65° are summarized in Table 1. We consider these angles sufficient for testing the ratio technique for nadir and off-nadir viewing angles. The slope shows the correlation between the visible and shortwave-IR reflectance, the standard deviation shows the variability of local reflectance, and the intercept gives the value of the visible reflectance when $R^{2.20}$ vanishes. Wen *et al.* [41] use this value in a method referred to as path radiance to derive aerosol optical thickness over dark surfaces for correlation coefficients ≥ 0.80.

For the blue ratio (see triangular symbols in Figure 1 and actual values in Table 1), the slope of $R^{0.68}$ as a function of $R^{2.20}$ is 0.169 at nadir and 1°, drops to 0.118 at 2°, oscillates between these two values for most zenith angles, and finally drops to 0.102 at 55° and 0.090 at 65°. A linear plot of the slope as a function of zenith angle clearly shows the variation from nadir to 65° (cf. Figure 2). In this figure, the vertical error bar at each zenith angle represents the standard deviation derived from the regression analysis shown in Figure 1, which are quite small in this case. Small variations as a function of zenith angle from nadir to 45° are clearly seen. For all zenith angles between nadir and 65° the intercept values vary from 0.02 to 0.07. For different instruments (Landsat TM and Airborne Visible and Infrared Imaging Spectrometer (AVIRIS)) and for different time periods, Kaufman *et al.* [19] obtained slopes between 0.13 and 0.30 and intercepts between –0.006 and 0.013. In fact, the slopes obtained from AVIRIS data over Hagerstown, Maryland and New Jersey during July 1993 are strikingly similar to the values reported in this study. Considering our data have not been corrected for atmospheric effects (absorption and scattering), it is noteworthy that our values are within the range of values reported in Table 1 of Kaufman *et al.* [19], differing very little from their average of 0.24. What happens after atmospheric ef-

fects are removed will become apparent in the next section.

Let us now look at the correlation between the red ($R^{0.68}$) and shortwave-IR ($R^{2.20}$) (cf. circular shaded symbols in Figure 1 and analyses summarized in Table 1). For all zenith angles the slope lies between 0.35 and 0.56, quite similar to the range of values reported by Kaufman *et al.* [19] for Landsat and AVIRIS data. A gradual increase in slope as a function of zenith angle is seen, reaching a maximum value at $\theta = 30°$ and gradually decreasing thereafter. The intercepts are quite small, in the range of 0.001 to 0.027, comparable to intercept values reported by Kaufman *et al.* [19].

From the above results, we conclude that the surface reflectance relationship $A_g^{0.47} = 0.25\,A_g^{2.20}$ given by Kaufman *et al.* [19] is not met for most zenith angles tested, whereas the relationship $A_g^{0.67} = 0.5\,A_g^{2.20}$ is met in a few cases; however, ratios approach the relationship suggested by Kaufman *et al.* [19] for zenith angles from nadir to 45°. We will examine these relationships further in the next section when we consider the compounding effects of atmospheric scattering on the measured earth-atmosphere reflection function measurements observed directly by the CAR.

In examining whether these relationships hold for other conditions, for example different solar geometry and atmospheric conditions, we analyzed data from other time series on August 18 where the solar illumination conditions were substantially different than those presented above. Between 19:18 and 19:23 UTC, the solar zenith angle $\theta_0 = 65.5°$ and the solar azimuth angle $\varphi_0 = 291.2°$. With the heading of the aircraft $H = 181.9°$ and with the CAR scanning on the right hand side of the aircraft, the relative azimuth angle $\varphi = 19.3°$. Most of the other conditions remain the same as those of the earlier time series, viz., clear weather conditions with low aerosol concentration having an aerosol optical

thickness $\tau_a \sim 0.08$ (at $\lambda = 0.55$ μm). In the blue channel and for all observational zenith angles, the slope lies between 0.038 and 0.11. In contrast, in the red channel, the slope lies between 0.23 and 0.39 (cf. Figure 3 and Table 2). Although the $\boldsymbol{R}^{2.20}$ values are small (< 0.25), the slope doesn't agree well with values suggested by Kaufman ***et al.*** [19].

In yet another flight section, between 19:41 and 19:45 UTC, $\theta_0 = 65.5°$, $\varphi_0 = 291.2°$, and the relative azimuth angle $\varphi = 17.3°$. For these data, the blue channel slopes lie in the range 0.04 to 0.08, and the red channel slope varies between 0.18 and 0.28 (cf. Table 3). These results show that despite the reflectance at 2.20 μm being small ($\boldsymbol{R}^{2.20} < 0.25$), the spectral ratio technique does not seem to hold well when viewing surfaces in the near-forward direction. In a previous study, Holben ***et al.*** [10] simulated both visible and near-infrared data from the Advanced Very High Resolution Radiometer (AVHRR) for a dark target, bare soil, and green-leaf biomass (low, medium, and high levels) and showed that viewing in the backscatter direction has more constant radiance with increasing scan angle than viewing in the forward scattering direction. Similarly, Remer ***et al.*** [32] pointed out that viewing in the forward scattering direction results in low correlation between visible and near-infrared reflectance. This probably explains the differences between backward and forward reflectance ratios.

On August 27 the University of Washington C-131A obtained CAR measurements near an AERONET sunphotometer site in Cuiabá, Mato Grosso, a part of Brazil that is much more affected by biomass burning and hence aerosol contamination than the region around Brasilia. On this day, the aerosol optical thickness $\tau_a \sim 0.68$ (at $\lambda = 0.55$ μm). We analyzed data from 19:02 to 19:08 UTC, during which time $\theta_0 = 54.1°$, $\varphi_0 = 295.1°$, $\varphi = 109.3°$, and the aircraft heading $\boldsymbol{H} = 95.8°$. The aircraft flew at an altitude of 2040 m above the ground. From the

voice log recorded during this flight, the atmosphere consisted of two thick smoke layers; the first layer was located between 270 and 2250 m, and the second between 2400 and 2700 m. There was a clear gap between the two layers that was confirmed by lidar measurements onboard the NASA ER-2 aircraft that overflew the area 45 min earlier.

The slope of $R^{0.47}$ as a function of $R^{2.20}$ varies from 0.05 to 0.09 for all zenith angles and those for $R^{0.68}$ as a function of $R^{2.20}$ from 0.20 to 0.34 (cf. Figure 4, Table 3). These values are substantially different from those recommended by Kaufman ***et al.*** [19]. Since the atmosphere was especially hazy during this flight, it is essential to do an atmospheric correction using the Second Simulation of the Satellite Signal in the Solar Spectrum (6S), a radiative transfer code described by Vermote ***et al.*** [40]. We will attempt to correct for the residual atmospheric effect, including gaseous absorption, for both this flight and the relatively clean flight near Brasilia on August 18 (described earlier), and determine the correlation between surface reflectance that remains after removing the effects of light scattering by the atmosphere.

VI. Atmospheric Correction

The 6S model allows us to determine the attenuation of solar irradiance under cloudless conditions at the surface. It removes the effects of Raleigh scattering, aerosol attenuation, and ozone and water vapor absorption, provided we know the key characteristics of the atmosphere, such as atmospheric optical thickness, etc. This is not practical for every CAR scan. However, CAR measurements on August 18 were made some 300 km NNW of a ground-based sun/sky radiometer site, and the more turbid conditions of August 27 were made essentially above a sun/sky radiometer located just outside Cuiabá. As a

consequence, some parameters of the atmosphere are available, thereby allowing us to perform atmospheric correction of the CAR radiometric observations. For each flight we assumed the input parameters for 6S were constant and unchanging.

The 6S code is a radiative transfer model based on the successive orders of scattering method. The spectral resolution of the model is 2.5 nm, and the aerosol layer is divided into 13 layers with a scale height of 2 km. The aerosol input for this model is the aerosol optical thickness at 0.55 μm ($\tau_a^{0.55}$), the aerosol size distribution, and the aerosol refractive index. We assumed the smoke aerosol model of Remer ***et al.*** [33] for the aerosol size distributions, a three mode lognormal model with modal radii of 0.132, 1.43 and 11.5 μm. The real refractive indices were assumed to be 1.43, 1.53 and 1.60—values representative of the range of real refractive index found for biomass burning aerosols [1], [26]. The imaginary part of the complex refractive index was fixed at 0.0035, 0.0046, and 0.005. These smoke size distributions were based on analysis of almucantar measurements made in cerrado and forest regions of Brazil. The aerosol optical depth at 0.55 μm was obtained by interpolating the measured τ_a^{λ} values between 0.50 and 0.67 μm. Also 6S computes the phase function, scattering and extinction coefficients (and single scattering albedo) from Mie theory as an output, based on these input aerosol parameters. Measurements of smoke particle shape in Brazil during SCAR-B, reported by Martins ***et al.*** [27], suggest that smoke in regional hazes over Amazonia consist largely of spherical particles, and thus, the use of the Mie calculations is appropriate.

Figure 5 shows the resultant ratios in the blue channel before and after the 6S correction was applied to CAR data on August 18 from 17:47–17:51 UTC for different values of $\tau_a^{0.55}$. Other than $\tau_a^{0.55}$ = 0.08, representing aerosol optical

thickness measured by the AERONET sunphotometer in Brasilia on this day, the other values of aerosol optical thickness $\tau_a^{0.55}$ = 0.0, 0.5, and 1.0 were arbitrarily chosen to show the sensitivity of optical thickness on the correlation between visible and shortwave-IR reflectance. As expected, the surface reflectance ratios after atmospheric correction are much greater than those before correction, and increase monotonically as a function of aerosol optical thickness. For all observational zenith angles, the slope of $A_g^{0.47}$ as a function of $A_g^{2.20}$ varies between 0.13 and 0.21 after atmospheric correction, which is still less than the average slope of 0.25 recommended by Kaufman ***et al.*** [19]. We note further that a significant drop in the surface reflectance ratio occurs for $\theta > 40°$, even after atmospheric correction. The decrease of k_0 for $\theta > 40°$ is not a surprise and we won't over emphasize it here, since it is a result of the increased path length of the atmosphere at larger viewing zenith angles. For $\tau_a^{0.55}$ = 0.0, the slope k_0 for the blue channel varies from 0.11 to 0.19 for all zenith angles. The slope increases as $\tau_a^{0.55}$ increases, with values ranging from 0.22 to 0.34 for $\tau_a^{0.55}$ = 0.5 and from 0.36 to 0.61 for $\tau_a^{0.55}$ = 1.0. We note that when $\tau_a^{0.55}$ = 0.5, the surface reflectance ratio ~ 0.25 for $0° \le \theta \le 40°$, as recommended by Kaufman ***et al.*** [19]. This is, however, not the atmospheric condition that apparently occurred at the time of these observations.

Figure 6 shows the slope of $A_g^{0.67}$ as a function of $A_g^{2.20}$ for all observational zenith angles after performing atmospheric correction. Values range from 0.37 to 0.68 for $\tau_a^{0.55}$ = 0.08, which corresponds to the aerosol optical thickness observed on this day. Considering error bars, the slopes seem to be approximately 0.5 for most of the range of zenith angles, in good agreement with [19]. The slopes clearly deviate from the 0.5 line for $\theta > 40°$. For $\tau_a^{0.55}$ = 0.0, the slopes vary from 0.32 to 0.59, and for $\tau_a^{0.55}$ = 0.5 the slopes lie between 0.61 and 0.99 for all zenith angles. The slopes are clearly above 1.0 for $\tau_a^{0.55}$ = 1.0 at all observational zenith

angles.

Atmospheric correction for the data obtained on August 27 between 19:02 and 19:08 UTC produces especially interesting results because of the large aerosol optical thickness observed on this day (cf. Figure 7). During this flight, the reflectance ratio in the blue channel was ~ 0.1 prior to atmospheric correction for all zenith angles $0° \leq \theta \leq 40°$, but jumps to around 0.25 after performing atmospheric correction where we assumed $\tau_a^{0.55} = 0.68$, as observed from a nearby AERONET sunphotometer on this day. In both the corrected and uncorrected data, the slope decreases for $\theta > 40°$, with an especially sharp decrease when $\theta > 55°$. Assuming $\tau_a^{0.55} = 0.0$, the slopes show a slight increase of ~ 0.01 from the slopes of the uncorrected data, which is quite insignificant compared to slopes obtained by assuming $\tau_a^{0.55} = 0.68$. In the red channel, shown in Figure 8, we see that the ratios substantially increase after atmospheric correction, as expected. Before atmospheric correction the slopes are ~ 0.1 for all zenith angles, and after correction, the slopes increase to between 0.7 and 0.8 at $\tau_a^{0.55} = 0.68$. With $\tau_a^{0.55} = 0.3$, the slopes approach the value recommended by Kaufman ***et al.*** [19], but this appears to be too low when the proper amount of atmospheric aerosol is taken into account. In contrast, at the 0.472 μm channel, the slopes correspond to the value recommended by Kaufman ***et al.*** [19] when $\tau_a^{0.55} = 0.68$.

VII. Azimuthal Variation

All cases considered thus far are for measurements obtained during straight and level flights, where we assumed that the azimuthal direction was invariant. In order to explore the azimuthal dependence of the spectral reflectance ratio technique, we analyzed bidirectional reflectance function (BRF) data collected over cerrado during SCAR-B [38] for August 18 from 18:51 to 19:02

UTC when θ_0 = 60.4°. The reflection function data were averaged over all azimuth angles at each zenith angle. The slopes of the azimuthally averaged reflectance for both blue and red channels increase with increasing zenith angle, quite different from what was observed for the straight and level flights (cf. Figure 9). In the blue channel the slopes varied from 0.06 around nadir to 0.22 at 55°, while in the red channel the slopes varied from 0.18 around nadir to 0.44 at 55°. These ratios gradually approach the values recommended by Kaufman ***et al.*** [19] the further one is away from nadir. Beyond 55°, the values, not shown in Figure 9, remain around the value attained at 55°, but the correlation coefficient deteriorates to below 0.50. Though no atmospheric corrections were applied to Figure 9, the effects of the atmosphere are small on this day (cf. Figures 5 and 6).

In order to examine the spectral reflectance measurements as well as the spectral ratios over all azimuthal angles, we have prepared polar plots, shown in Figure 10, that illustrate the distribution of reflectance over all azimuthal angles at each of three wavelengths: (a) 0.47, (b) 0.68, and (c) 2.20 μm. The ratios $R^{0.47}/R^{2.20}$ and $R^{0.68}/R^{2.20}$ are shown in Figures 10d and e, while Figure 10f shows the ratio $R^{0.47}/R^{0.68}$ for different view geometries. In all polar plots, the observational zenith angle is represented by the radial distance from the center of the circle and the azimuth angle is represented as the length of arc on the respective zenith circle. The principal plane (i.e., the vertical plane containing the sun) resides in the 0-180° azimuth direction with the sun located in the 180° azimuth direction. With this definition, the upper half circle represents forward scattering and the lower half circle represents backward scattering. For the three CAR channels presented here, the BRF appears symmetric about the principal plane and the smoothest at 0.47 μm. The spectral BRF for the visible wavelengths is less than 0.25 for all zenith angles except for the anti-solar point located near θ

= 60.4° and φ = 180° in the 0.68 μm channel. At 2.20 μm, the reflection function is less than 0.3 except in the anti-solar direction (hotspot), where $R^{2.20} > 0.4$. The ratios, shown in Fig 10d and e, are generally invariant along azimuthal direction, being primarily a function of view zenith angle. The small variability noted along different circles in the azimuthal direction may largely be attributed to surface effects. In the 0.47 μm channel $R^{0.47}/R^{2.20} > 0.15$, whereas at 0.68 μm the ratio $R^{0.68}/R^{2.20} > 0.4$. In Figure 10e, $R^{0.68}/R^{2.20}$ shows very small difference in reflectance above a zenith angle of 60°.

Finally, we analyzed BRF data acquired over dense forest on August 27 that took place between 19:17-19:23 UTC over a forested area northwest of Cuiabá (Figure 11). In all three channels, the spectral reflectance was symmetrical and < 0.2, an indication of a dark target (dense dark vegetation). For $0° < \theta < 60°$, the spectral reflectance ratio lies between 0.3 and 0.5, which is quite similar to the value recommended by Kaufman *et al.* [19] for the 0.68 μm channel. At 0.47 μm, on the other hand, the reflectance ratio $R^{0.47}/R^{2.20} > 0.3$, which is much larger than the value recommended by Kaufman *et al.* [19]. None of the results presented in Figures 10 or 11 have had atmospheric correction applied.

VIII. Summary and Conclusions

We have used the Cloud Absorption Radiometer (CAR) multispectral, multiangular data, collected during the Smoke, Clouds, and Radiation–Brazil (SCAR-B) experiment, to examine the surface reflectance ratio technique that is an underlying assumption in the remote sensing of tropospheric aerosols over the land from the Moderate Resolution Imaging Spectroradiometer (MODIS), as described by Kaufman *et al.* [19] and King *et al.* [22] for all zenith angles from nadir to 65°. The strategy we adopted was to first select a low turbidity flight over

cerrado of Brazil on August 8, 1995 and to compute reflectance ratios at 0.47 and 0.68 μm to corresponding measurements at 2.20 μm, separately accounting for backward and forward scattering directions. Similarly, we analyzed data from August 27, 1995 in a more turbid environment not far from the city of Cuiabá in Mato Grosso, Brazil. For both flights, we removed the effects of atmospheric absorption and scattering using 6S, a radiative transfer code developed by Vermote ***et al.*** [40], where we recomputed the spectral ratios for various values of aerosol optical thickness. Finally, we analyzed bidirectional reflectance function (BRF) data to examine the dependence of the reflectance ratio technique on relative azimuth angle.

Results of this analysis show that, once the atmosphere is removed from the spectral reflectance measurements, the resulting slopes of $R^{0.47}$ as a function of $R^{2.20}$ lies between 0.18 and 0.27 for zenith angles from nadir to 55°, dropping to as low as 0.08 at $\theta = 65°$ (cf. Figures 5 and 7). The variation with zenith angle is small and the correlation remains above 0.80 for $\theta < 45°$, which is an indication of a good linear fit. The intercept, obtained by regression of $R^{0.47}$ as a function of $R^{2.20}$, is quite small and can thus be largely ignored. For a good linear relationship, the intercept should be zero, i.e., if there is no surface reflectance in the 2.20 μm channel, then there should be none in the 0.47 μm channel, an assumption built into Kaufman ***et al.'s*** [19] correlation approach. However, Wen ***et al.*** [41] found that the intercept of $R^{0.47}$ and $R^{0.68}$ as a function of $R^{2.20}$ can be used to derive the aerosol optical thickness of the scene. It is interesting to note that the reflectance ratio technique uses a specific value of the slope to derive the optical thickness over dense dark vegetation targets (defined as pixels for which $R^{2.20} \leq 0.1$ or $R^{2.20} \leq 0.25$). The path radiance technique, on the other hand, first establishes the existence of a relationship at the surface between visible and short-

wave-IR reflectance, and assumes that the same relationship holds at the top of the atmosphere. Under this assumption, Wen et al. [41] derive the aerosol optical thickness from the intercept where the shortwave-IR vanishes. The slopes of $R^{0.68}$ as a function of $R^{2.20}$ lies between 0.352 and 0.554 for $\theta < 55°$. The intercept for the linear fit $R^{0.68}$ as a function of $R^{2.20}$ is an order of magnitude smaller than the fit of $R^{0.47}$ against $R^{2.20}$ for most zenith angles, an indication that the model is better suited to this wavelength. Higher correlation ($r > 0.80$) at most zenith angles further serves to show the goodness of the linear fit at this wavelength.

In the case of measurements taken in the forward scattering direction, the slopes of $R^{0.47}$ as a function of $R^{2.20}$ are slightly less than 0.1 for most zenith angles and the correlation is slightly less than 0.80 for most cases and considerably worse at 65° off-nadir ($r \sim 0.19$). The variability of the spectral ratio for $\theta < 40°$ is small, suggesting the possibility that the values can be modeled by a simple parameter with some tolerable degree of uncertainty. The slopes of $R^{0.68}$ as a function of $R^{2.20}$ lies between 0.233 and 0.473, lower than for measurements made in the backscattering direction, at most zenith angles. The correlation falls below 0.80, to as low as 0.28, at $\theta = 65°$. Although the variability of the spectral slopes of $R^{0.68}$ as a function $R^{2.20}$ are greater than the corresponding slopes of $R^{0.47}$ as a function of $R^{2.20}$ for all zenith angles from nadir to 40°, the slopes of $R^{0.68}$ as function of $R^{2.20}$ seems to oscillate around a value of 0.3, an indication that a relationship can be developed for these zenith angles.

In the case where measurements were obtained in a more turbid atmosphere where the aerosol optical thickness $\tau_a^{0.55} = 0.68$, the slopes of $R^{0.47}$ as a function of $R^{2.20} \sim 0.1$ for zenith angles from nadir to 40° with very little variability as a function of zenith angle (cf. Figure 4). This case is quite similar to the one for forward scattering discussed above, and suggests that the two cases may

be parameterized by a simple relationship. The slopes of $\boldsymbol{R}^{0.68}$ as a function of $\boldsymbol{R}^{2.20} \sim 0.34$ for zenith angles up to 40° with correspondingly small variability between zenith angles. The correlation coefficient is generally somewhat less than 0.80 at 0.47 μm and somewhat greater than 0.80 at 0.68 μm (cf. Table III).

After atmospheric corrections are applied to the raw reflection function measurements, the reflectance slopes increase, with the greatest increase occurring for the largest aerosol optical thickness.

In the case of azimuthally averaged BRF data, the slopes increase as a function of viewing zenith angle, being the greatest the further away from nadir as one views a scene, at least out to $\theta = 55°$, beyond which the correlation coefficients are too low to yield any useful relationship. The reflectance ratios show little variation with azimuth angle, being especially well behaved in the backward scattering directions over dark targets (cf. Figures 10 and 11).

It is clear from the above discussion that a relationship between visible reflectance and shortwave infrared reflectance exists for zenith angles from nadir to about 40°, and that a simple parametric relationships can be derived. In light of these observations, the relationship $\boldsymbol{R}^{0.47} = 0.25\boldsymbol{R}^{2.20}$ does not seem to hold for the cases tested here, but the relationship $\boldsymbol{R}^{0.68} = 0.5\boldsymbol{R}^{2.20}$ seems to hold fairly well for zenith angles from nadir to 45°, a good indication of its potential use in the remote sensing of tropospheric aerosol optical properties from spaceborne observations.

ACKNOWLEDGEMENT

This research was supported by funding provided by the MODIS Science Team, the EOS Project Science Office, and NASA's Radiation Science Program.

REFERENCES

[1] B. E. Anderson, W.B. Grant, G. L. Gregory, E. V. Browell, J. E. Collins, G. W. Sachse, D. R. Bagwell, C. H. Hudgins, D. R. Blake, and N. J. Blake, "Aerosols from biomass burning over the tropical South Atlantic region: Distribution and impacts," ***J. Geophys. Res.,*** vol. 101, pp. 24117–24138, 1996.

[2] G. T. Arnold, M. D. King, S. C. Tsay, J. Y. Li, and P. F. Soulen, "Airborne spectral measurements of surface-atmosphere anisotropy for Arctic sea ice and tundra," ***Int. J. Remote Sens.,*** in press, 2000.

[3] R. A. Bryson, "A perspective on climate change," ***Science***, vol. 184, pp. 753–760, 1974.

[4] S. Chandrasekhar, ***Radiative Transfer***, Dover, 393 pp.

[5] R. A. Ferrare, R. S. Fraser, and Y.J. Kaufman, "Satellite measurements of large scale air pollution: Measurements of forest fire smoke," ***J. Geophys. Res.***, vol. 92, pp. 9911–9925, 1990.

[6] R. S. Fraser, "Satellite measurement of mass of Sahara dust in the atmosphere," ***Appl. Opt.***, vol. 15, pp. 2471–2479, 1976.

[7] R. S. Fraser, and Y. J. Kaufman, "The relative importance of aerosol scattering and absorption in remote sensing," ***IEEE Trans. Geosci. Remote Sens.,*** vol. 23, pp. 625–633, 1985.

[8] R. S. Fraser, Y. J. Kaufman, and R. L. Mahoney, "Satellite measurements of aerosol mass and transport," ***Atmos. Environ.***, vol. 18, pp. 2577–2584, 1984.

[9] M. Griggs, "Satellite measurements of tropospheric aerosols," ***Adv. Space Res***., vol. 2, pp. 109–118, 1983.

[10] B. N. Holben, and R. S. Fraser, "Red and near-infrared sensor response to off-nadir viewing," ***Int. J. Remote Sens***., vol. 5, pp. 145–160, 1984.

[11] B. N. Holben, T. F. Eck, I. Slutsker, D. Tanré, J. P. Buis, A. Setzer, E. Ver-

mote, J. A. Reagan, Y. J. Kaufman, T. Nakajima, F. Lavenu, I. Jankowiak, and A. Smirnov, "AERONET—A federated instrument network and data archive for aerosol characterization," ***Remote Sens. Environ.***, vol. 66, pp. 1–16, 1998.

[12] B. N. Holben, E. Vermote, Y. J. Kaufman, D. Tanré, and V. Kalb, "Aerosol retrieval over land from AVHRR data—Application for atmospheric correction," ***IEEE Trans. Geosci. Remote Sens.***, vol. 30, pp. 12–222, 1992.

[13] R. B. Husar, J. M. Prospero, and L. L. Stowe, "Characterization of tropospheric aerosols over the oceans with the NOAA advanced very high resolution radiometer optical thickness operational product," ***J. Geophys. Res.***, vol. 102, pp. 16889–16909, 1997.

[14] M. Kästner, P. Koepke, and H. Quenzel, "Monitoring of the Saharan dust over the Atlantic using METEOSAT-Vis-Data," ***Adv. Space Res.***, vol. 2, pp. 119–121, 1983.

[15] Y. J. Kaufman, "Measurements of the aerosol optical thickness and the path radiance—Implications on aerosol remote sensing and atmospheric corrections, ***J. Geophys. Res.,*** vol. 98, pp. 2677–2692, 1993.

[16] Y. J. Kaufman, and L. A. Remer, "Detection of forests using mid-IR reflectance: An application for aerosol studies," ***IEEE Trans. Geosci. Remote Sens.***, vol. 32, pp. 672–683, 1994.

[17] Y. J. Kaufman, and C. Sendra, "Algorithm for automatic atmospheric corrections to visible and near-IR satellite imagery," ***Int. J. Remote Sens.***, vol. 9, pp. 1357–1381, 1988.

[18] Y. J. Kaufman, R. S. Fraser, and R. A. Ferrare, "Satellite measurements of large-scale air pollution: Method," ***J. Geophys. Res.***, vol. 95, pp. 9895–9909, 1990.

[19] Y. J. Kaufman, A. E. Wald, L. A. Remer, B. C. Gao, R. R. Li, and L. Flynn, "The MODIS 2.1-μm channel-correlation with visible reflectance for use in remote sensing of aerosol," ***IEEE Trans. Geosci. Remote Sens.***, vol. 35, pp. 1286–1298, 1997.

[20] Y. J. Kaufman, P. V. Hobbs, V. W. J. H. Kirchhoff, P. Artaxo, L. A. Remer, B. N. Holben, M. D. King, D. E. Ward, E. M. Prins, K. M. Longo, L. F. Mattos, C. A. Nobre, J. D. Spinhirne, Q. Ji, A. M. Thompson, J. F. Gleason, S. A. Christopher and S. C. Tsay, "The Smoke, Clouds, and Radiation—Brazil (SCAR-B) experiment," ***J. Geophys. Res***., vol. 103, pp. 31783–31808, 1998.

[21] M. D. King, and D. D. Herring, "Monitoring Earth's vital signs," ***Sci. Amer***., vol. 282, pp. 72–77, 2000.

[22] M. D. King, Y. J. Kaufman, D. Tanré, and T. Nakajima, "Remote sensing of aerosols from space: Past, present, and future," ***Bull. Amer. Meteor. Soc***., vol. 80, pp. 2229–2259, 1999.

[23] M. D. King, M. G. Strange, P. Leone, and L. R. Blaine, "Multiwavelength scanning radiometer for airborne measurements of scattered radiation within clouds," ***J. Atmos. Oceanic Tech.***, vol. 3, pp. 513–522, 1986.

[24] P. Koepke, and H. Quenzel, "Turbidity of the atmosphere determined from satellite: Calculation of optimum viewing geometry," ***J. Geophys. Res***., vol. 84, pp. 7847–7856, 1979.

[25] P. Koepke, and H. Quenzel, "Turbidity of the atmosphere determined from satellite: Calculation of optimum wavelength," ***J. Geophys. Res***., vol. 86, pp. 9801–9805, 1981.

[26] J. Lenoble, "The particulate matter from biomass burning: A tutorial and critical review of its radiative impact," in ***Global Biomass Burning: Atmospheric, Climatic, and Biospheric Implications***, edited by J. S. Levine, pp.

381–386, MIT Press, Cambridge, Mass., 1991.

[27] J. V. Martins, P. Artaxo, P. V. Hobbs, C. Liousse, H. Cachier, Y. J. Kaufman, and A. Plana-Fattori, "Particle size distributions, elemental composition, carbon measurements, and optical properties of smoke from biomass burning in the Pacific Northwest of the United States," in ***Biomass Burning and Global Change***, edited by J. S. Levine, pp. 716–732, MIT Press, Cambridge, Mass., 1996.

[28] R. A. McCormick, and J. H. Ludwig, "Climate modification by atmospheric aerosols," ***Science***, vol. 156, pp. 1358–1359, 1967.

[29] Y. Mekler, H. Quenzel, G. Ohring, and I. Marcus, "Relative atmospheric aerosol content from ERTS observations," ***J. Geophys. Res.***, vol. 82, pp. 967–970, 1977.

[30] T. Nakajima, and A. Higurashi, "AVHRR remote sensing of aerosol optical properties in the Persian Gulf region, summer 1991," ***J. Geophys. Res.***, vol. 102, pp. 16935–16946, 1997.

[31] S. I. Rasool, and S. H. Schneider, "Atmospheric carbon dioxide and aerosols: Effects and large increases on global climate," ***Science***, vol. 173, pp. 138–141, 1971.

[32] L. A. Remer, A. E. Ward, and Y. J. Kaufman, "Angular and seasonal variation of spectral ratios: Implications for the remote sensing of aerosol over land," ***IEEE Trans. Geosci. Remote Sens.***, submitted, 2000.

[33] L. A. Remer, S. Gasso, D. A. Hegg, Y. J. Kaufman, and B. N. Holben, "Urban/Industrial aerosol: Ground-based sun/sky radiometer and airborne in situ measurements," ***J. Geophys. Res.***, vol. 102, pp. 16849–16859, 1997.

[34] S. W. Running, C. O. Justice, V. Salomonson, D. Hall, J. Barker, Y. J. Kaufman, A. H. Strahler, A. R. Huete, J. P. Muller, V. Vanderbilt, Z. M. Wan, P.

Teillet, and D. Carneggie, "Terrestrial remote sensing science and algorithms planned for EOS/MODIS," ***Int. J. Remote Sens.***, vol. 15, pp. 3587–3620, 1994.

[35] L. L. Stowe, A. M. Ignatov, and R. R. Singh, "Validation and potential enhancement to the second-generation operational aerosol product at the National Environmental Satellite, Data and information Service of the National Oceanic and Atmospheric Administration," ***J. Geophys. Res.***, vol. 102, pp. 16923–16934, 1997.

[36] P. F. Soulen, M. D. King, S. C. Tsay, G. T. Arnold, and J. Y. Li, "Airborne spectral measurements of surface-atmosphere anisotropy during the SCAR-A, Kuwait oil fire, and TARFOX experiments," ***J. Geophys. Res***., vol. 105, pp. 10203–10218, 2000.

[37] D. Tanré, Y. J. Kaufman, M. Herman, and S. Mattoo, "Remote sensing of aerosol properties over oceans using the MODIS/EOS spectral radiance," ***J. Geophys. Res***., vol. 102, pp. 16971–16988, 1997.

[38] S. C. Tsay, M. D. King, G. T. Arnold, and J. Y. Li, "Airborne spectral measurements of surface anisotropy during SCAR-B," ***J. Geophys. Res***., vol. 103, pp. 31943–31954, 1998.

[39] H. C. van de Hulst, ***Multiple Light Scattering, Tables, Formulas, and Applications***, Vol. 1. New York: Academic Press, pp. 76–82, 1980.

[40] E. F. Vermote, D. Tanré, J. L. Deuzé, M. Herman, and J. J. Morcrette, "Second simulation of the satellite signal in the solar spectrum, 6S: An overview," ***IEEE Trans. Geosci. Remote Sens.***, vol. 35, pp. 675–686, 1997.

[41] G. Wen, S. C. Tsay, R. F. Cahalan, and L. Oreopoulos, "Path radiance technique for retrieving aerosol optical thickness over land," ***J. Geosci. Res.***, vol. 104, pp. 31321–31332, 1999.

Charles K. Gatebe received the B.Sc. (meteorology, mathematics, and physics) and M.Sc. (meteorology) degrees from the University of Nairobi, Kenya, in 1990 and 1994, respectively, and the Ph.D. degree in atmospheric sciences from the University of Witwatersrand, South Africa, in 1999. He holds the position of Lecturer in the Institute of Nuclear Science, University of Nairobi, where he teaches courses on air pollution using nuclear related techniques. He came to NASA Goddard Space Flight Center in 1999 as a Resident Research Associate of the Universities Space Research Association (USRA). He is currently an atmospheric scientist in the Goddard Earth Science and Technology Center, University of Maryland Baltimore County, and is on leave from his faculty position in Kenya.

His research experience includes developing a simple gaussian model to estimate motor vehicle emissions from line sources (highways) in Nairobi, in situ measurements of aerosols and gases, and characterizing aerosol sources using statistical and trajectory methods. He has been involved in International Atomic Energy Agency (IAEA) coordinated research project on air pollution using nuclear related analytic techniques and in 1994/95 was a member of the United Nations Environmental Programme (UNEP)/World Health Organization (WHO), Global Environmental Monitoring System (GEMS)/Air team of experts. Currently, Dr Gatebe is interested in remote sensing of aerosols and clouds to better understand their role in climate variability and change. He is also involved with modification of NASA's Cloud Absorption Radiometer to have modern data acquisition system and UV optical channels suitable for remote sensing of aerosol.

Most recently Dr Gatebe has won the 2000 World Meteorological Organization Young Scientist Award.

Michael D. King received the B.A. degree in physics from Colorado College in 1971, and the M.S. and Ph.D. degrees in atmospheric sciences from the University of Arizona in 1973 and 1977, respectively.

He is Senior Project Scientist of NASA's Earth Observing System (EOS), where he has primary responsibility for providing scientific insight and guidance to the EOS Project management and for representing the EOS Project to the Earth science community. He is currently a Goddard Senior Fellow at NASA Goddard Space Flight Center, where he has worked since joining NASA in January 1978. He is a member of the MODIS and CERES Science Teams of EOS, and has been the leader of the atmosphere discipline group of MODIS since 1989. His research experience includes conceiving, developing, and operating multispectral scanning radiometers from a number of aircraft platforms in field experiments ranging from arctic stratus clouds off Barrow, Alaska, to smoke from the Kuwait oil fires in the Persian Gulf, biomass burning in the cerrado of Brazil and southern Africa. Earlier, he developed the Cloud Absorption Radiometer for studying the absorption properties of optically thick clouds as well as the bidirectional reflectance properties of many natural surfaces.

Dr. King has been recognized several times by NASA for his achievements, including receiving the NASA Exceptional Service Medal in 1985 and the NASA Exceptional Scientific Achievement Medal in 1992. He received an Honorary ***Doctor of Science*** degree from Colorado College in 1995, is a Fellow of the American Meteorological Society, and has been awarded the 1992 Transactions Prize Paper Award by the IEEE Geoscience and Remote Sensing Society. He is also a recipient of the Verner E. Suomi Award of the AMS for 'significant and fundamental contributions to remote sensing and radiative transfer, and for leadership in spacecraft experiments.' Dr King is an adjunct Professor of Oceanography at

Dalhousie University.

Si-Chee Tsay received the B.S. degree in atmospheric science from the National Taiwan University in 1977, and the M.S. and Ph.D. degrees in atmospheric science from the University of Alaska in 1982 and 1986, respectively. After four years as a Research Associate at Colorado State University, he came to NASA Goddard Space Flight Center as a USRA Resident Research Associate. He joined NASA Goddard Space Flight Center as an atmospheric scientist in 1994.

His early work focused on numerically stable methods for calculating light scattering in multiple scattering and emitting layered media using the discrete ordinates method of radiative transfer. This led to the development of the popular, and widely used, software code known as DISORT. More recently, his research experience includes science planning and operation of multispectral scanning radiometers from aircraft platforms in field experiments for the purpose of studying aerosol, cloud, and surface properties. He has used the Cloud Absorption Radiometer and MODIS Airborne Simulator onboard research aircraft to aid in the development of atmospheric and land remote sensing and retrieval algorithms under NASA's Earth Observing System projects, and has been a leader in developing a sophisticated set of surface-based radiation instrumentation for validation of satellite data.

Q. Ji received the B.S. degree in atmospheric science from Peking University in 1983, the M.S. degree in aerodynamics from Beijing Institute of Electromechanical Engineering in 1986, and the Ph.D. degree in atmospheric science from the University of Alaska in 1996. He joined Science Systems and Applications Inc., NASA Goddard Space Flight Center, as a Senior Scientist in 1996, working under the NASA Global Monitoring of Aerosol Properties project and the NASA Global

Aerosol Climatology Project.

His research experience includes designing, developing and operating the Cloud Condensation Nuclei (CCN) Remover for measuring CCN; and utilizing ground-based remote sensing instrumentation for making solar, infrared and microwave radiation measurements of the uatmosphere.

G. Thomas Arnold received the B S. degree in meteorology from the State University of New York College at Oswego in 1981 and the M.S. degree in atmospheric science from the University of Wyoming in 1986.

His research experience includes processing, calibrating and analyzing data from aircraft-based multispectral scanning radiometers deployed in field experiments to study aerosol, cloud, and surface properties. These radiometers include the Multichannel Cloud Radiometer, the Cloud Absorption Radiometer and the MODIS Airborne Simulator. He has also written software to read and analyze aircraft in-situ microphysical data for validation of remote sensing (radiometer) data. More recently he has begun an effort to visualize MODIS Airborne Simulator cloud mask data over the arctic and research how to best use the cloud mask data to determine thermodynamic phase.

Jason Y. Li received the B.A. degree in applied physics (with honors) in 1991 from Curtin University of Technology, Perth, Australia, and the M.S. degree in atmospheric and oceanic sciences in 1993 from the University of Wisconsin-Madison. Currently, he is a senior program analyst with the Emergent Information Technology Inc.

His research experience includes processing and analyzing Cloud Absorption Radiometer data, studying BRDF characteristics for various surfaces, remote sensing of clouds, and scientific data visualization. He is also an active partici-

pant in field experiments.

Table I

SLOPE, INTERCEPT, AND CORRELATION COEFFICIENT (***r***) FOR ZENITH ANGLES FROM NADIR TO 65° COMPUTED FROM REGRESSION OF REFLECTANCE AT BLUE (0.47 μm) AND RED (0.68 μm) VS. REFLECTANCE AT 2.20 μm FOR DATA FROM AUGUST 18, 1995, 1747-1751 UTC. FOR EACH ZENITH ANGLE THE NUMBER OF VALUES USED IN THE REGRESSION IS INDICATED IN COLUMN 2.

Zenith Angle (°)	Points Used	Slope ± standard deviation		Intercept		***r***	
		Blue	Red	Blue	Red	Blue	Red
0	48	0.169± 0.008	0.445± 0.022	0.023	0.006	0.927	0.952
1	48	0.169± 0.008	0.503± 0.025	0.023	-0.002	0.899	0.917
2	51	0.118± 0.006	0.372± 0.017	0.030	0.015	0.894	0.917
3	51	0.128± 0.007	0.390± 0.021	0.028	0.011	0.917	0.929
4	51	0.117± 0.007	0.353± 0.019	0.030	0.017	0.876	0.868
5	51	0.148± 0.006	0.477± 0.026	0.026	0.001	0.864	0.884
6	51	0.140± 0.007	0.457± 0.020	0.026	0.002	0.850	0.925
7	49	0.110± 0.007	0.352± 0.018	0.031	0.017	0.840	0.900
8	51	0.130± 0.007	0.395± 0.022	0.029	0.012	0.879	0.896
9	50	0.121± 0.006	0.366± 0.017	0.030	0.016	0.867	0.868
10	51	0.153± 0.007	0.460± 0.022	0.026	0.004	0.879	0.907
15	51	0.128± 0.006	0.394± 0.020	0.029	0.009	0.891	0.896
20	50	0.154± 0.009	0.507± 0.039	0.028	-0.001	0.917	0.926
30	51	0.169± 0.010	0.563± 0.032	0.030	-0.009	0.921	0.924
40	51	0.178± 0.012	0.544± 0.035	0.034	-0.005	0.942	0.936
45	51	0.155± 0.009	0.468± 0.027	0.039	0.005	0.919	0.916
55	51	0.102± 0.005	0.354± 0.017	0.057	0.027	0.763	0.764
65	51	0.090± 0.004	0.312± 0.014	0.071	0.036	0.775	0.802

Table II

SLOPE, INTERCEPT, AND CORRELATION COEFFICIENT (*r*) FOR ZENITH ANGLES FROM NADIR TO 65° COMPUTED FROM REGRESSION OF REFLECTANCE AT BLUE (0.47 μm) AND RED (0.68 μm) VS. REFLECTANCE AT 2.20 μm FOR DATA FROM AUGUST 18, 1995, 1918–1923 UTC. FOR EACH ZENITH ANGLE THE NUMBER OF VALUES USED IN THE REGRESSION IS INDICATED IN COLUMN 2.

Zenith Angle (°)	Points Used	Slope ± standard deviation		Intercept		*r*	
		Blue	Red	Blue	Red	Blue	Red
0	57	0.102± 0.005	0.334± 0.017	0.011	0.028	0.839	0.774
1	57	0.076± 0.004	0.270± 0.015	0.032	0.023	0.726	0.794
2	57	0.089± 0.005	0.372± 0.019	0.03	0.009	0.684	0.806
3	57	0.075± 0.004	0.261± 0.012	0.032	0.022	0.503	0.533
4	57	0.060± 0.003	0.233± 0.012	0.033	0.024	0.505	0.584
5	57	0.095± 0.005	0.383± 0.019	0.028	0.006	0.728	0.782
6	57	0.092± 0.004	0.395± 0.019	0.03	0.008	0.708	0.778
7	57	0.094± 0.006	0.385± 0.026	0.03	0.01	0.806	0.831
8	57	0.073± 0.004	0.312± 0.018	0.032	0.018	0.63	0.64
9	57	0.061± 0.004	0.268± 0.017	0.033	0.02	0.652	0.701
10	57	0.098± 0.005	0.394± 0.021	0.029	0.003	0.787	0.808
15	57	0.110± 0.007	0.473± 0.031	0.028	-0.007	0.846	0.917
20	57	0.082± 0.004	0.295± 0.015	0.03	0.014	0.69	0.773
30	57	0.075± 0.004	0.309± 0.016	0.035	0.016	0.72	0.797
40	57	0.109± 0.006	0.340± 0.017	0.037	0.017	0.741	0.824
45	57	0.068± 0.003	0.242± 0.011	0.048	0.033	0.533	0.651
55	57	0.029± 0.001	0.198± 0.009	0.071	0.047	0.239	0.654
65	57	-0.042± 0.001	0.081± 0.003	0.119	0.085	0.191	0.276

Table III

SLOPE, INTERCEPT, AND CORRELATION COEFFICIENT (***r***) FOR ZENITH ANGLES FROM NADIR TO 65° COMPUTED FROM REGRESSION OF REFLECTANCE AT BLUE (0.47 μm) AND RED (0.68 μm) VS. REFLECTANCE AT 2.20 μm FOR DATA FROM AUGUST 27, 1995, 1902–1908 UTC. FOR EACH ZENITH ANGLE THE NUMBER OF VALUES USED IN THE REGRESSION IS INDICATED IN COLUMN 2.

Zenith Angle (°)	Points Used	Slope ± standard deviation		Intercept		***r***	
		Blue	Red	Blue	Red	Blue	Red
0	75	0.088± 0.006	0.336± 0.024	0.047	0.024	0.796	0.883
1	75	0.093± 0.006	0.358± 0.023	0.047	0.020	0.798	0.892
2	75	0.096± 0.007	0.313± 0.022	0.046	0.028	0.838	0.903
3	75	0.092± 0.006	0.319± 0.022	0.047	0.028	0.796	0.888
4	75	0.089± 0.006	0.302± 0.021	0.048	0.030	0.837	0.902
5	75	0.097± 0.006	0.326± 0.021	0.046	0.025	0.855	0.896
6	75	0.090± 0.006	0.333± 0.020	0.047	0.024	0.793	0.890
7	75	0.087± 0.006	0.301± 0.020	0.048	0.031	0.838	0.895
8	75	0.093± 0.006	0.324± 0.022	0.048	0.028	0.813	0.884
9	75	0.094± 0.007	0.325± 0.024	0.047	0.027	0.868	0.924
10	75	0.106± 0.008	0.339± 0.025	0.045	0.023	0.904	0.913
15	75	0.105± 0.008	0.340± 0.024	0.046	0.024	0.893	0.930
20	75	0.091± 0.006	0.322± 0.022	0.050	0.028	0.826	0.899
30	75	0.091± 0.005	0.331± 0.020	0.054	0.029	0.805	0.895
40	75	0.089± 0.005	0.354± 0.021	0.062	0.027	0.751	0.892
45	75	0.075± 0.005	0.310± 0.020	0.070	0.037	0.741	0.905
55	75	0.068± 0.003	0.265± 0.013	0.087	0.054	0.563	0.822
65	75	0.025± 0.001	0.250± 0.014	0.120	0.069	0.240	0.886

Table IV

SLOPE, INTERCEPT, AND CORRELATION COEFFICIENT (*r*) FOR ZENITH ANGLES FROM NADIR TO 65° COMPUTED FROM REGRESSION OF REFLECTANCE AT BLUE (0.47 μm) AND RED (0.68 μm) VS. REFLECTANCE AT 2.20 μm FOR A BRDF FLIGHT ON AUGUST 18, 1995, 1851–1902 UTC. FOR EACH ZENITH ANGLE THE NUMBER OF VALUES USED IN THE REGRESSION IS INDICATED IN COLUMN 2.

Zenith Angle (°)	Points Used	Slope ± standard deviation		Intercept		*r*	
		Blue	Red	Blue	Red	Blue	Red
0	327	0.071± 0.003	0.205± 0.008	0.032	0.041	0.521	0.561
1	327	0.065± 0.002	0.189± 0.008	0.033	0.043	0.509	0.527
2	327	0.082± 0.003	0.232± 0.009	0.030	0.036	0.581	0.608
3	327	0.086± 0.004	0.247± 0.010	0.030	0.034	0.625	0.665
4	327	0.082± 0.003	0.243± 0.010	0.030	0.035	0.586	0.648
5	327	0.072± 0.003	0.229± 0.009	0.032	0.036	0.596	0.614
6	327	0.081± 0.004	0.239± 0.010	0.030	0.033	0.617	0.627
7	327	0.092± 0.004	0.274± 0.012	0.029	0.028	0.645	0.668
8	327	0.092± 0.004	0.276± 0.012	0.029	0.029	0.651	0.666
9	327	0.099± 0.004	0.296± 0.013	0.028	0.026	0.648	0.687
10	327	0.089± 0.004	0.274± 0.011	0.029	0.030	0.628	0.641
15	327	0.112± 0.005	0.315± 0.014	0.026	0.023	0.695	0.715
20	327	0.119± 0.005	0.305± 0.013	0.025	0.025	0.684	0.687
30	327	0.134± 0.007	0.339± 0.017	0.026	0.024	0.685	0.734
40	327	0.176± 0.010	0.396± 0.022	0.021	0.016	0.805	0.814
45	327	0.187± 0.009	0.383± 0.019	0.023	0.020	0.744	0.743
55	327	0.214± 0.014	0.446± 0.028	0.026	0.015	0.834	0.845
65	75	0.025± 0.001	0.250± 0.014	0.120	0.069	0.240	0.886

FIGURE LEGENDS

Fig. 1. Scatter plots of reflectance $R^{0.47}$ and $R^{0.68}$ as a function of reflectance $R^{2.20}$ for views angles: (a) 0°, (b) 10°, (c) 20°, (d) 30°, (e) 40°, and (f) 65°. The relative azimuth $\varphi = 132.1°$.

Fig. 2. Slopes from regression of $R^{0.47}$ and $R^{0.68}$ against $R^{2.20}$ as a function of zenith angle for cerrado northwest of Brasilia, when $\theta_0 = 45.4°$ and $\varphi = 132.1°$.

Fig. 3. Slopes from regression of $R^{0.47}$ and $R^{0.68}$ against $R^{2.20}$ as a function of zenith angle for cerrado northwest of Brasilia, when $\theta_0 = 45.4°$ and $\varphi = 65.5°$.

Fig. 4. Slopes from regression of $R^{0.47}$ and $R^{0.68}$ against $R^{2.20}$ as a function of zenith angle corrected for various levels of aerosol optical depth near Cuiabá, when $\theta_0 = 54.1°$ and $\varphi = 109.3°$.

Fig. 5. Slopes from regression of $R^{0.47}$ against $R^{2.20}$ as a function of zenith angle corrected for various values of aerosol optical thickness. These observations were acquired northwest of Brasilia when $\theta_0 = 45.4°$ and $\varphi = 132.1°$.

Fig. 6. Slopes from regression of $R^{0.68}$ against $R^{2.20}$ as a function of zenith angle corrected for various values of aerosol optical thickness. These observations were acquired northwest of Brasilia when $\theta_0 = 45.4°$ and $\varphi = 132.1°$.

Fig. 7. Slopes from regression of $R^{0.47}$ against $R^{2.20}$ as a function of zenith angle corrected for various values of aerosol optical thickness. These observations were acquired near Cuiabá when $\theta_0 = 54.1°$ and $\varphi = 109.3°$.

Fig. 8. Slopes from regression of $R^{0.68}$ against $R^{2.20}$ as a function of zenith angle corrected for various values of aerosol optical thickness. These observations were acquired near Cuiabá when $\theta_0 = 54.1°$ and $\varphi = 109.3°$.

Fig. 9. Azimuthally averaged reflectance ratios $R^{0.47}/R^{2.20}$ and $R^{0.68}/R^{2.20}$ as a

function of zenith angle near Cuiabá, when $\theta_0 = 60.4°$.

Fig. 10. Spectral measurements of the surface-atmosphere system bidirectional reflectance over cerrado northwest of Brasilia on August 18, 1995 for (a) $\boldsymbol{R}^{0.47}$, (b) $\boldsymbol{R}^{0.68}$, (c) $\boldsymbol{R}^{2.20}$, (d) $\boldsymbol{R}^{0.47}/\boldsymbol{R}^{2.20}$, (e) $\boldsymbol{R}^{0.68}/\boldsymbol{R}^{2.20}$, and (f) $\boldsymbol{R}^{0.47}/\boldsymbol{R}^{0.68}$. In all of these plots the solar zenith angle was 60.4°.

Fig. 11. Spectral measurements of the surface-atmosphere system bidirectional reflectance over dense forest on August 25, 1995 for (a) $\boldsymbol{R}^{0.47}$, (b) $\boldsymbol{R}^{0.68}$, (c) $\boldsymbol{R}^{2.20}$, (d) $\boldsymbol{R}^{0.47}/\boldsymbol{R}^{2.20}$, (e) $\boldsymbol{R}^{0.68}/\boldsymbol{R}^{2.20}$, and (f) $\boldsymbol{R}^{0.47}/\boldsymbol{R}^{0.68}$. In all of these plots the solar zenith angle was 56.7°.

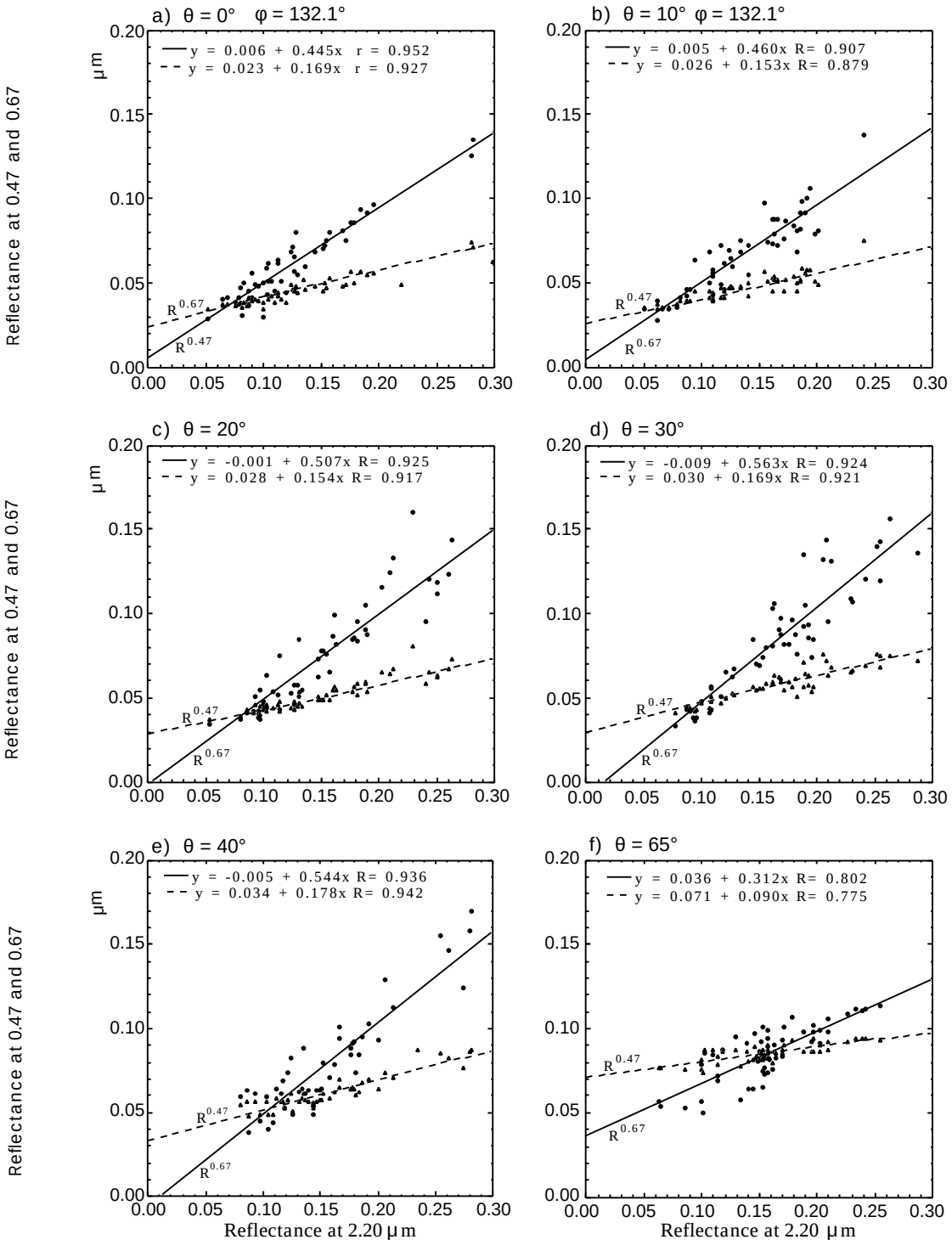

Figure 1. Scatter plots of reflectance $R^{0.47}$ and $R^{0.68}$ as a function of reflectance $R^{2.20}$ for views angles: (a) 0°, (b) 10°, (c) 20°, (d) 30°, (e) 40°, and (f) 65°. The relative azimuth φ = 132.1°.

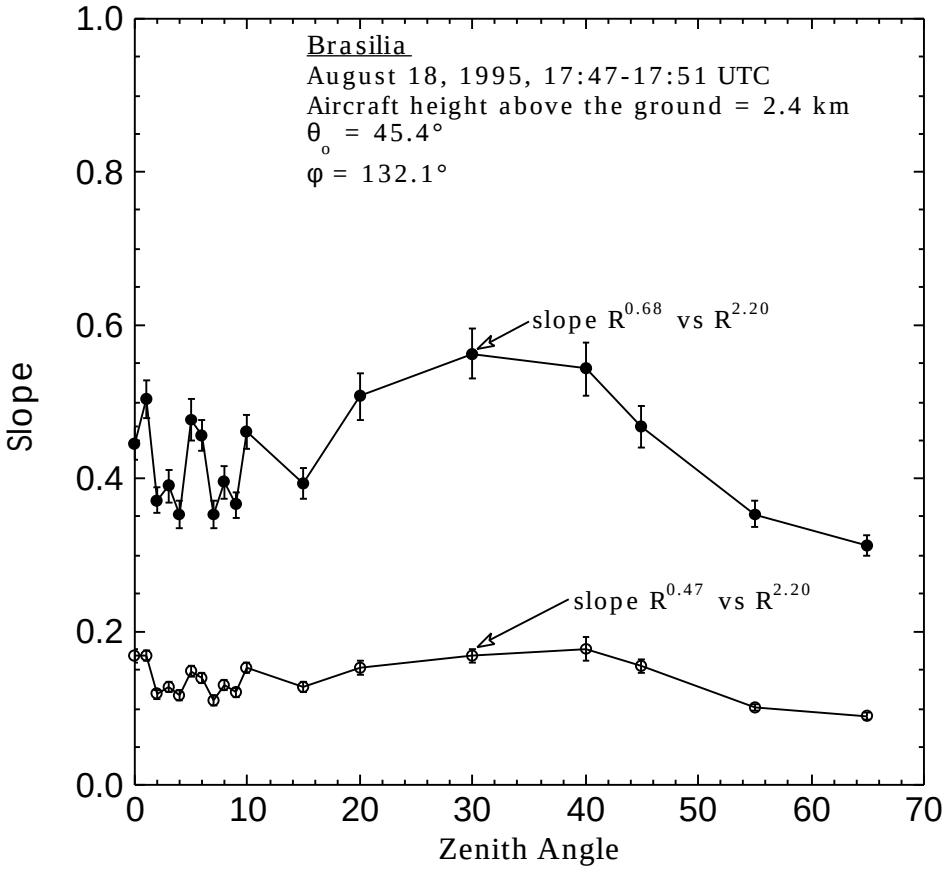

Figure 2. Slopes from regression of $\boldsymbol{R}^{0.47}$ and $\boldsymbol{R}^{0.68}$ against $\boldsymbol{R}^{2.20}$ as a function of zenith angle for cerrado northwest of Brasilia, when $\theta_0 = 45.4°$ and $\varphi = 132.1°$.

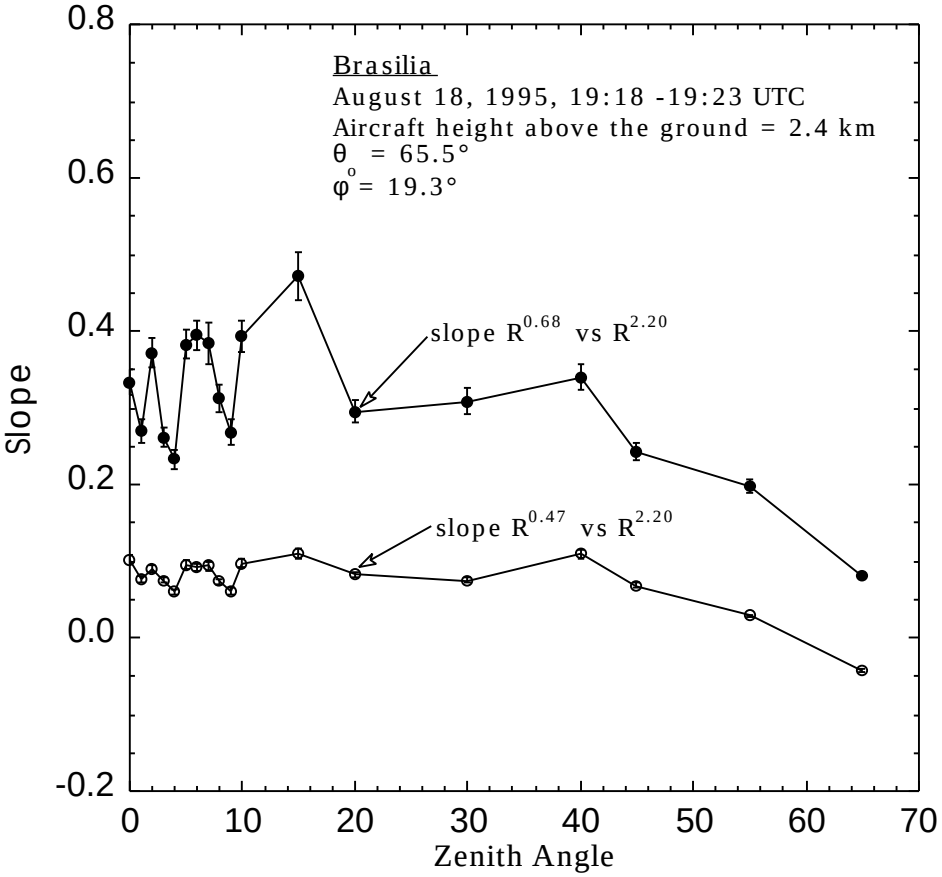

Figure 3. Slopes from regression of $R^{0.47}$ and $R^{0.68}$ against $R^{2.20}$ as a function of zenith angle for cerrado northwest of Brasilia, when $\theta_0 = 45.4°$ and $\varphi = 65.5°$.

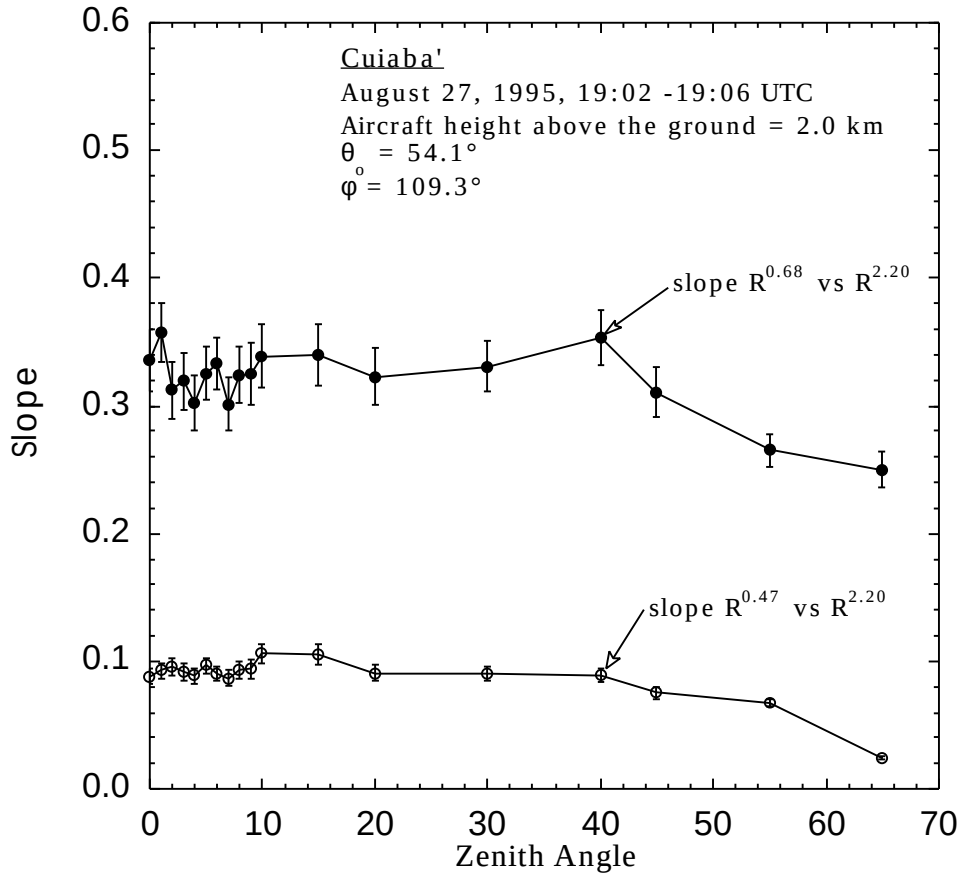

Figure 4. Slopes from regression of $\boldsymbol{R}^{0.47}$ and $\boldsymbol{R}^{0.68}$ against $\boldsymbol{R}^{2.20}$ as a function of zenith angle corrected for various levels of aerosol optical depth near Cuiabá, when $\theta_0 = 54.1°$ and $\varphi = 109.3°$.

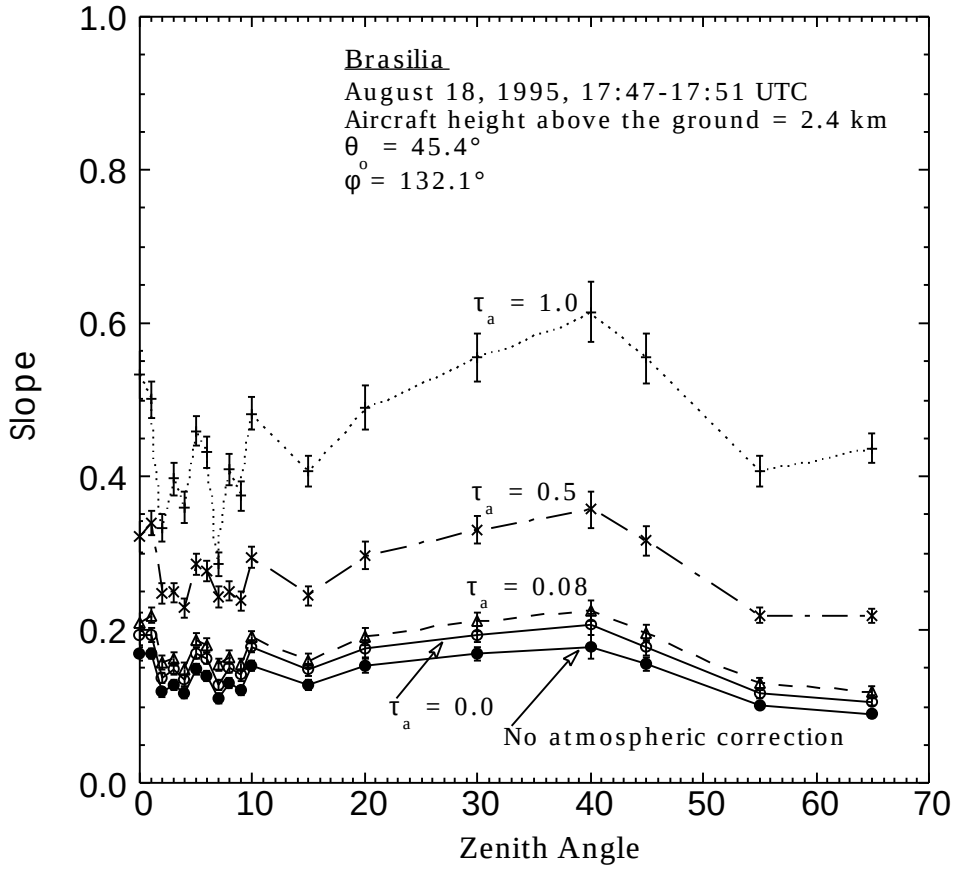

Figure 5. Slopes from regression of $R^{0.47}$ against $R^{2.20}$ as a function of zenith angle corrected for various values of aerosol optical thickness. These observations were acquired northwest of Brasilia when $\theta_0 = 45.4°$ and $\varphi = 132.1°$.

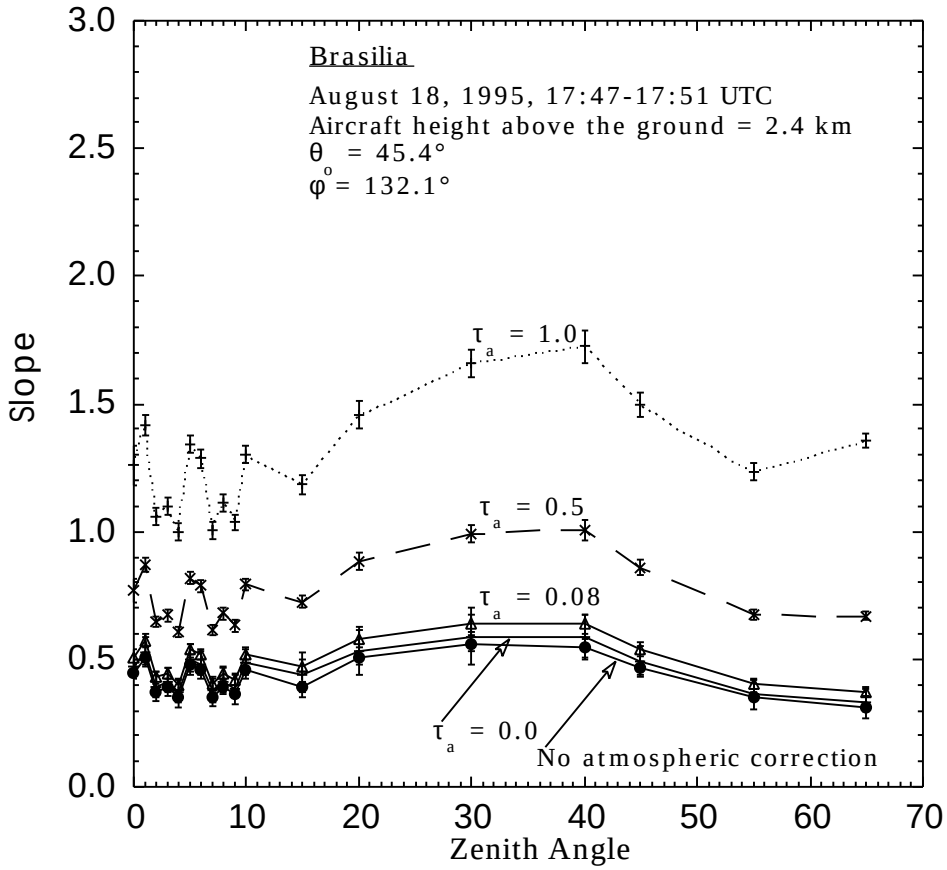

Figure 6. Slopes from regression of $R^{0.68}$ against $R^{2.20}$ as a function of zenith angle corrected for various values of aerosol optical thickness. These observations were acquired northwest of Brasilia when $\theta_0 = 45.4°$ and $\varphi = 132.1°$.

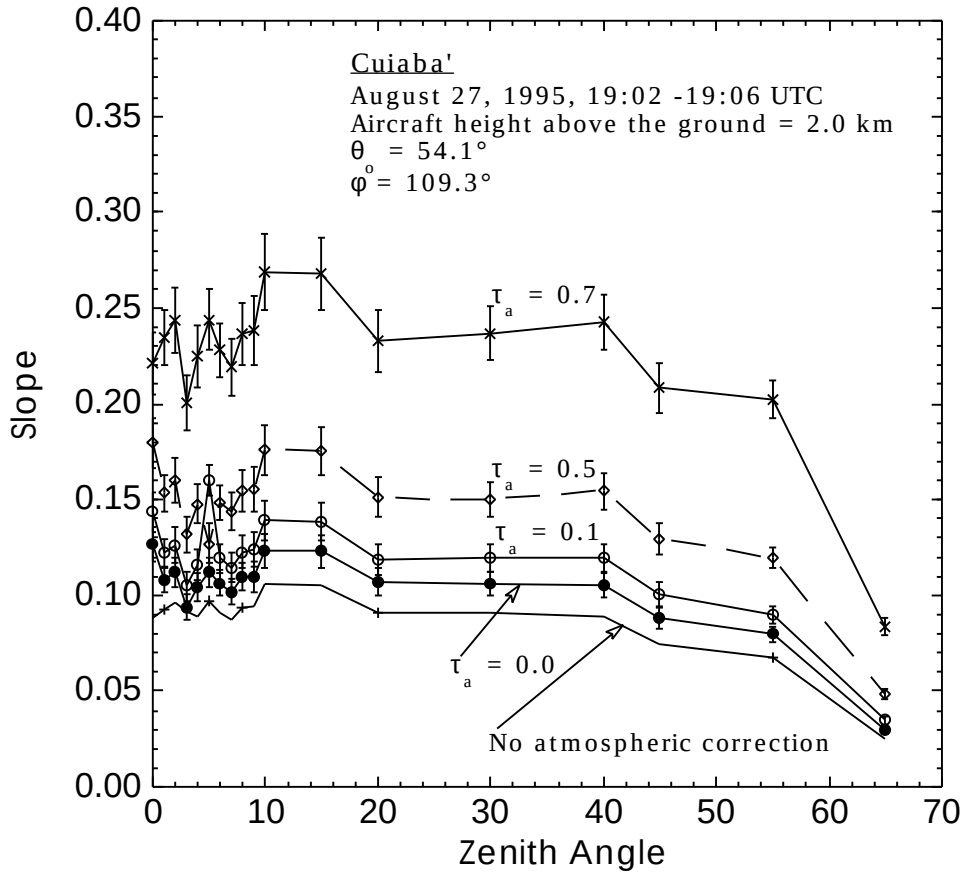

Figure 7. Slopes from regression of $\boldsymbol{R}^{0.47}$ against $\boldsymbol{R}^{2.20}$ as a function of zenith angle corrected for various values of aerosol optical thickness. These observations were acquired near Cuiabá when $\theta_0 = 54.1°$ and $\varphi = 109.3°$.

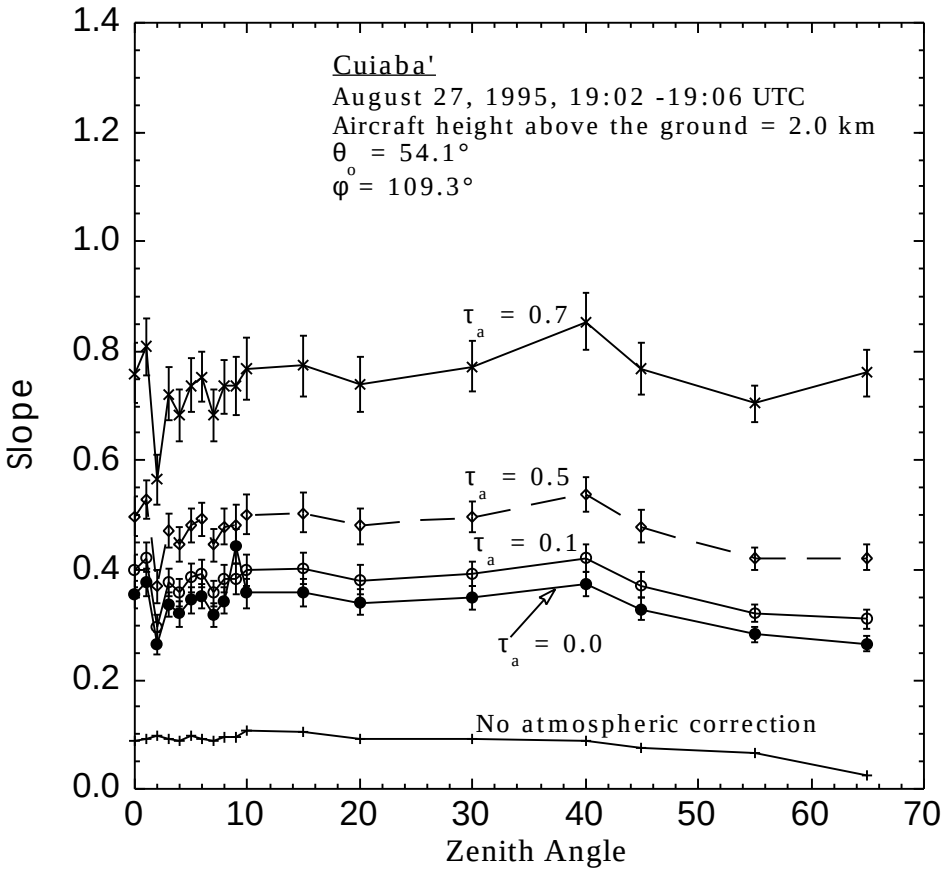

Figure 8. Slopes from regression of $\boldsymbol{R}^{0.47}$ against $\boldsymbol{R}^{2.20}$ as a function of zenith angle corrected for various values of aerosol optical thickness. These observations were acquired near Cuiabá when $\theta_0 = 54.1°$ and $\varphi = 109.3°$.

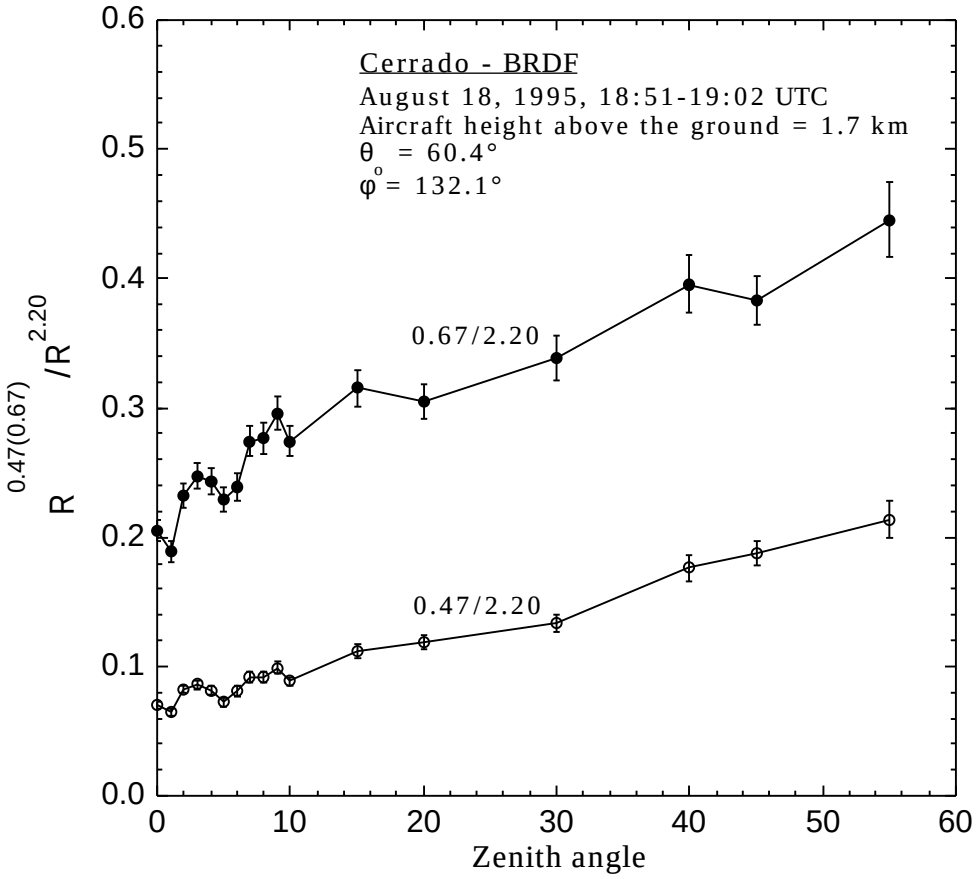

Figure 9. Azimuthally averaged reflectance ratios $\boldsymbol{R}^{0.47}/\boldsymbol{R}^{2.20}$ and $\boldsymbol{R}^{0.68}/\boldsymbol{R}^{2.20}$ as a function of zenith angle near Cuiabá, when $\theta_0 = 60.4°$.

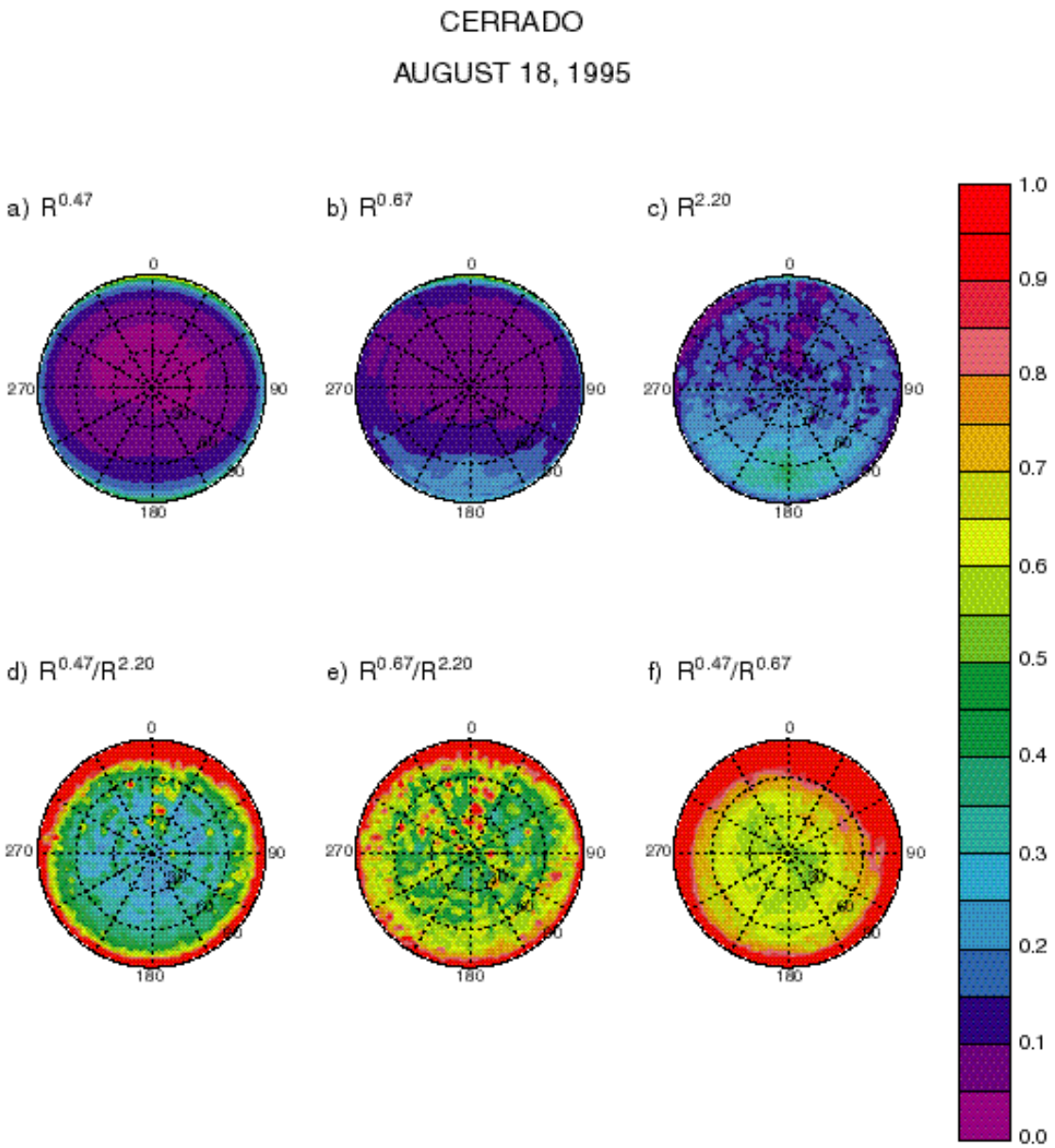

Figure 10 Spectral measurements of the surface-atmosphere system bidirectional reflectance over cerrado northwest of Brasilia on August 18, 1995 for (a) $\boldsymbol{R}^{0.47}$, (b) $\boldsymbol{R}^{0.68}$, (c) $\boldsymbol{R}^{2.20}$, (d) $\boldsymbol{R}^{0.47}/\boldsymbol{R}^{2.20}$, (e) $\boldsymbol{R}^{0.68}/\boldsymbol{R}^{2.20}$, and (f) $\boldsymbol{R}^{0.47}/\boldsymbol{R}^{0.68}$. In all of these plots the solar zenith angle was 60.4°.

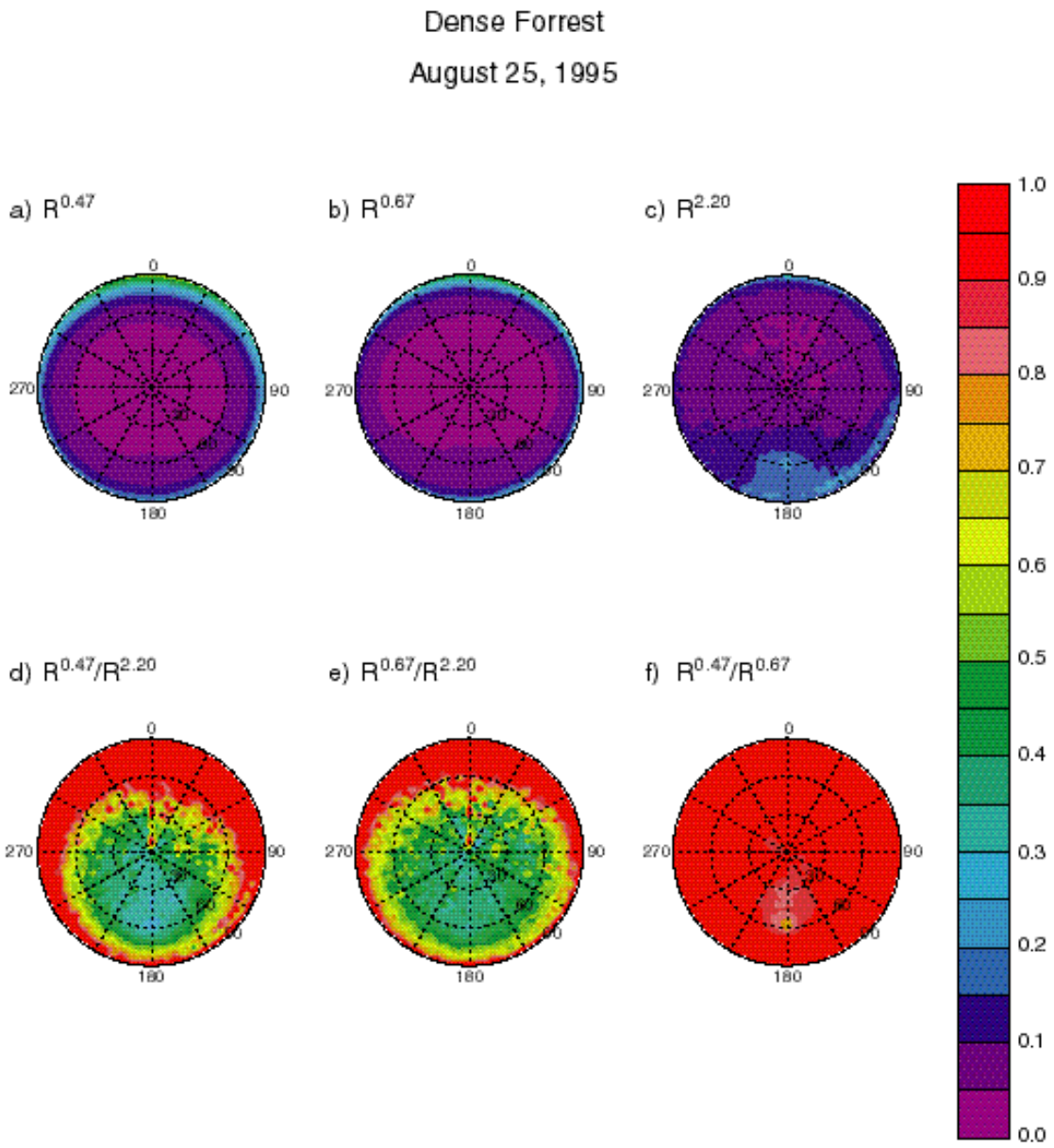

Figure 11. Spectral measurements of the surface-atmosphere system bidirectional reflectance over dense forest on August 25, 1995 for (a) $\boldsymbol{R}^{0.47}$, (b) $\boldsymbol{R}^{0.68}$, (c) $\boldsymbol{R}^{2.20}$, (d) $\boldsymbol{R}^{0.47}/\boldsymbol{R}^{2.20}$, (e) $\boldsymbol{R}^{0.68}/\boldsymbol{R}^{2.20}$, and (f) $\boldsymbol{R}^{0.47}/\boldsymbol{R}^{0.68}$. In all of these plots the solar zenith angle was 56.7°.